

RESEARCH ARTICLE

10.1002/2013JE004527

Key Points:

- Space weathering rapidly alters the UV slope of moderate- to high-iron soils
- In the highlands the 321/415 nm ratio is largely controlled by shock and melting
- Micrometeorite bombardment alone may be an inefficient agent of space weathering

Correspondence to:

B. W. Denevi,
brett.denevi@jhuapl.edu

Citation:

Denevi, B. W., M. S. Robinson, A. K. Boyd, H. Sato, B. W. Hapke, and B. R. Hawke (2014), Characterization of space weathering from Lunar Reconnaissance Orbiter Camera ultraviolet observations of the Moon, *J. Geophys. Res. Planets*, 119, 976–997, doi:10.1002/2013JE004527.

Received 11 SEP 2013

Accepted 7 APR 2014

Accepted article online 22 APR 2014

Published online 7 MAY 2014

Characterization of space weathering from Lunar Reconnaissance Orbiter Camera ultraviolet observations of the Moon

Brett W. Denevi¹, Mark S. Robinson², Aaron K. Boyd², Hiroyuki Sato², Bruce W. Hapke³, and B. Ray Hawke⁴
¹Johns Hopkins University Applied Physics Laboratory, Laurel, Maryland, USA, ²School of Earth and Space Exploration, Arizona State University, Tempe, Arizona, USA, ³Department of Geology and Planetary Sciences, University of Pittsburgh, Pittsburgh, Pennsylvania, USA, ⁴Hawaii Institute of Geophysics and Planetology, University of Hawaii, Honolulu, Hawaii, USA

Abstract We investigate the effects of space weathering at ultraviolet wavelengths using a near-global seven-band (321–689 nm) mosaic from the Lunar Reconnaissance Orbiter Camera (LROC) Wide Angle Camera (WAC). We confirm that for moderate- to high-iron compositions (≥ 5 wt % FeO), the steeply positive UV slope at wavelengths <415 nm shallows with increasing exposure to space weathering. We measure these differences in LROC WAC data as variations in the 321/415 nm ratio, which has low values for fresh craters in the mare and moderate-iron highlands. For low-iron highland compositions, the break in slope occurs at shorter wavelengths, and it is instead the 321/360 nm ratio that increases with exposure to the space-weathering environment, whereas the 321/415 nm ratio appears to be largely controlled by the degree of shock experienced during the impact. The effects of shock may be more important at highland craters because modest shock pressures result in the solid-state transformation of plagioclase to its glass equivalent, maskelynite, and can help distinguish between primary shocked ejecta and locally exposed fresh material in rays. While all of the “fresh” craters we examined have UV spectral properties consistent with substantial alteration due to space weathering, the UV spectra of lunar swirls (magnetically shielded from the solar wind) are consistent with exposure of immature, crystalline material. Together these results suggest that lunar space weathering is dominated by the solar wind and “saturates” in the UV at I_0/FeO values of ~ 40 (submature).

1. Introduction

Because the Moon lacks an atmosphere and a global magnetic field, its surface is constantly bombarded by charged particles from the solar wind and galactic cosmic rays and by micrometeoroids. Exposure to this rain of charged particles and small impactors results in physical and chemical changes in the lunar regolith that are collectively referred to as space weathering. These changes include (1) comminution of coherent material into finer particles, (2) sputtering and vaporization of material that is redeposited on soil particles as thin, amorphous coatings, which contain submicroscopic-size metallic iron (SMFe, also called nanophase iron or npFe^0) grains [e.g., Hapke et al., 1975; Keller and McKay, 1993, 1997; Pieters et al., 2000a; Hapke, 2001; Sasaki et al., 2001; Noble et al., 2007], and (3) the formation of glass-welded agglomerates of regolith particles known as agglutinates [Wells and Hapke, 1977; Taylor et al., 2001, 2010; Blewett et al., 2011b]. These changes affect the reflectance of a surface as a function of wavelength, and both complicate the interpretation of compositional information from reflectance spectra and provide an opportunity to assess a surface’s “maturity,” or its time exposed to the space-weathering environment.

It is now well known that the optical properties of submicroscopic iron are largely responsible for the differences in reflectance (increase in spectral slope, decrease in overall reflectance and reduction of spectral contrast) observed with increasing exposure to space weathering. Laboratory experiments have shown that irradiating powders of comminuted silicate rocks with simulated solar wind causes atoms to be sputtered (knocked loose) from particle surfaces and then redeposited as a thin coating on nearby soil particles [e.g., Hapke, 1966, 1973; Yin et al., 1972, 1975; Hapke et al., 1975; Yin and Tsang, 1976]. Heating and vaporization of lunar soil particles by micrometeoroid impacts, which can be simulated in the laboratory using an electron beam furnace [Hapke et al., 1975] or a high-powered laser [e.g., Yamada et al., 1999; Sasaki et al., 2001], also results in thin coatings on soil particles. For both sputter-deposited and vapor-deposited coatings, various

factors, including the atomic weight and binding energies of atoms, result in these coatings being preferentially enriched in iron and depleted in oxygen (see discussion in *Hapke* [2001]). Thus, ferrous iron is reduced to iron metal, and both sputter deposition (from solar wind irradiation) and vapor deposition (from micrometeoroid impacts) produce SMFe-bearing particles, but the relative contributions of each of these two processes and the attendant implications for rates of weathering are not well known.

Agglutinates are also thought to play a role in altering the spectral properties of lunar soils. These glassy particles can make up half the volume of mature soils and are low in reflectance (reflectance <5% at 750 nm) and relatively spectrally neutral [see *Pieters et al.*, 1993, Figure 3]. Agglutinates are formed by impact melting and mixing of older generations of the regolith, so that the mineral and glass fragments within are not pristine, but are already space weathered themselves (and in fact agglutinates contain older generations of agglutinates). Hence SMFe that would normally be restricted to surface coatings is distributed throughout the volume of agglutinates [*Hapke et al.*, 1975; *Kerridge*, 1994; *Hapke*, 2001] and is larger in size (>10 nm compared to <5 nm) [*Keller et al.*, 1998]. While glass itself is not necessarily low in reflectance [e.g., *Wells and Hapke*, 1977], agglutinitic glass hosting this larger size fraction of SMFe is. Metallic Fe particles smaller than the wavelength reduce reflectance primarily at visible and near-infrared wavelengths, resulting in a reddening of the spectrum, and the main effect of particles larger than the wavelength, such as those found in agglutinates, is to decrease reflectance across the visible and near-infrared [*Pieters et al.*, 1993; *Britt and Pieters*, 1994; *Noble et al.*, 2007; *Lucey and Riner*, 2011].

Remote sensing-based studies of the maturation of the lunar regolith typically employ visible and near-infrared (VIS-NIR) reflectance spectroscopy [e.g., *Fischer and Pieters*, 1994; *Lucey et al.*, 2000a]. At VIS-NIR wavelengths (approximately 400–2000 nm), an increased abundance of SMFe is manifested as an increase in spectral slope, a decrease in overall reflectance, and a reduction in crystal field absorption band depth. Ultraviolet (UV) wavelengths are also useful for studying space weathering. Silicates typically exhibit a steep decrease in reflectance toward UV wavelengths (<450 nm) due to strong charge-transfer absorption bands below ~300 nm [e.g., *Wells and Hapke*, 1977]. Comparisons of laboratory spectra of powdered lunar rocks (unweathered) and mature lunar soil samples suggest that the steep UV slope (from ~200 to 450 nm) of silicates is reduced in weathered soils [*Hendrix and Vilas*, 2006], and telescopic spectra show a stronger UV slope for fresh craters relative to mature soil [*Pieters*, 1977]. Though this trend is the opposite of that seen in the VIS-NIR (spectra become flatter or more blue in the UV rather than steeper and more red in the VIS-NIR), it is also likely due to the addition of SMFe, which is comparatively spectrally neutral [*Allen et al.*, 1996; *Hapke*, 2001]. Differences in far-UV (<200 nm) spectra have also been attributed to space weathering [*Hendrix et al.*, 2012].

While changes in reflectance across ultraviolet-visible wavelengths due to space weathering have been investigated with laboratory spectra of lunar soils and via comparisons of meteorite and asteroid spectra [*Hendrix and Vilas*, 2006], the effects of space weathering have yet to be examined across the lunar surface for regions of varying maturity. Here we use global ultraviolet and visible image data to examine maturity trends at these shorter wavelengths with implications for the rates and causes of lunar space weathering.

2. Data and Methods

Multispectral images from the Lunar Reconnaissance Orbiter Camera (LROC) Wide Angle Camera (WAC) provide the means to assess the effects of space weathering on the UV reflectance of lunar soils. The WAC is a pushframe imager with seven narrow band-pass filters [*Robinson et al.*, 2010]. Ultraviolet and visible filters share a single CCD, but are imaged through separate optics. UV images are obtained through two filters at 321 and 360 nm (32 and 15 nm full-width half-maximum, respectively) and have a cross-track field of view (FOV) of 60°. To increase the signal-to-noise ratio, UV images are binned on-chip (4 by 4) for a nadir resolution of ~380 m/pixel from a 50 km orbit. Five visible filters (415, 566, 604, 643, and 689 nm) are imaged with a nadir resolution of ~75 m/pixel from a 50 km orbit. The visible optics have a FOV of 90°, though in color mode only the center ~60° are read from the CCD. All filters are exposed simultaneously and 14 lines by 704 samples of each visible filter and 16 lines by 512 samples (summed on chip to 4 lines by 128 samples) of each UV filter are read out. Continuous coverage is obtained by imaging at regular intervals consistent with spacecraft groundspeed.

The large range of viewing angles within a single WAC observation ($\pm 30^\circ$ emission and phase) requires a robust photometric correction. The images are corrected to a standard photometric geometry (incidence, emission, and phase angles of 30° , 0° , and 30°) using an empirical function derived from WAC data at each wavelength [Boyd *et al.*, 2012] with illumination and viewing angles calculated from the global lunar digital terrain model with a sampling scale of 100 m (GLD100) [Scholten *et al.*, 2012]. The WAC acquires near-global coverage of the Moon each month, and the mosaic used here was created by photometrically correcting ~ 20 months of data (over 65,000 color mode images), binning the normalized reflectance by geographic location, and taking the median value at each bin. This process increases the signal-to-noise ratio by taking advantage of the WAC's repeat coverage (the average number of observations per pixel is 84) and has the benefit of an associated standard deviation at each pixel representing the error due to residual uncorrected photometric effects or calibration artifacts [Boyd *et al.*, 2012]. The resulting seven-band mosaic covers $\pm 60^\circ$ latitude at a pixel scale of 400 m.

To assess changes in UV slope due to maturity differences, we focus on the short wavelength region of the WAC data, particularly the 321, 360, and 415 nm filters. This region of the spectrum is affected by the strong decrease in reflectance associated with fresh silicates, and we can assess changes in reflectance due to exposure to the space-weathering environment. While SMFe is expected to decrease the slope in this wavelength region and thus increase the 321/415 nm ratio [Hendrix and Vilas, 2006], variations in mineral and glass constituents also affect UV reflectance. Titanium, in particular, has a strong effect on the UV/visible ratio [e.g., Charette *et al.*, 1974; Wells and Hapke, 1977]. The addition of ilmenite (FeTiO_3), a spectrally neutral opaque mineral, to a mixture increases the 321/415 nm ratio (see spectra of ilmenite-rich (>6 vol %) Apollo 11 and 17 samples, Figure 1b), while the strong charge-transfer absorptions in titanium-rich glasses (nonagglutinitic) can have the opposite effect. For this reason, it is informative to compare the reflectance of immature material with that of mature material of same composition.

For comparison to the LROC WAC lunar data, we examine laboratory spectra of soils from the lunar soil characterization consortium (LSCC) [Taylor *et al.*, 2001, 2010], which span a range of maturities and compositions. The maturity of laboratory soils can be quantified as I_s/FeO , a value that normalizes the ferromagnetic resonance of a soil (related to SMFe content) to the total FeO content of the soil [Morris, 1976, 1978]. All I_s/FeO values are given for the <250 μm fraction. We also analyze spectra of lunar soils and powdered rocks from Wagner *et al.* [1987], with powdered rocks providing an unweathered end-member (assumed I_s/FeO value of zero). To add to our sampling of unweathered materials, we also compare two additional spectra of powdered lunar rocks from the Reflectance Experiment Laboratory (RELAB) database [Pieters and Hiroi, 2004]. In addition, because most immature material is exposed by impact craters, which subject materials to varying degrees of shock, we examine spectra of synthetic glasses [Wells, 1977; Blewett *et al.*, 2011b] and maskelynite [Pieters, 1996], a diaplectic plagioclase glass. For each laboratory spectrum, the reflectance data is convolved to the LROC WAC band passes by taking the mean within the full-width half maximum of each WAC filter [Robinson *et al.*, 2010].

For further comparison to our LROC WAC UV data, we use an empirical model of maturity derived from Clementine visible and near-infrared multispectral images known as the optical maturity (OMAT) parameter [Lucey *et al.*, 1995, 2000a]. OMAT is based on a surface's reflectance at 750 nm versus its 950/750 nm ratio; a high OMAT value is consistent with a less mature surface (OMAT is inversely correlated with I_s/FeO) [Lucey *et al.*, 2000a].

Finally, we supplement our 400 m pixel scale WAC observations with high-resolution LROC Narrow Angle Camera (NAC) images. These broadband NAC images have pixel scales as small as 0.25 m, and allow for a detailed comparison between the various facies of crater ejecta (impact melt, blocky ejecta, and fine-grained ejecta deposits) and differences in 321/415 nm ratio. Overlaying WAC color images on the higher-resolution NAC images facilitates this comparison; in these cases WAC mosaics were resampled using both nearest neighbor (to preserve individual pixel values) and bilinear interpolation.

3. Results

3.1. Maturity Trends in the UV From Laboratory Spectra

The well-characterized samples of the lunar soil characterization consortium [Taylor *et al.*, 2001, 2010] provide an opportunity to understand the variation in UV spectral properties for soils of known levels of maturity (I_s/FeO), for

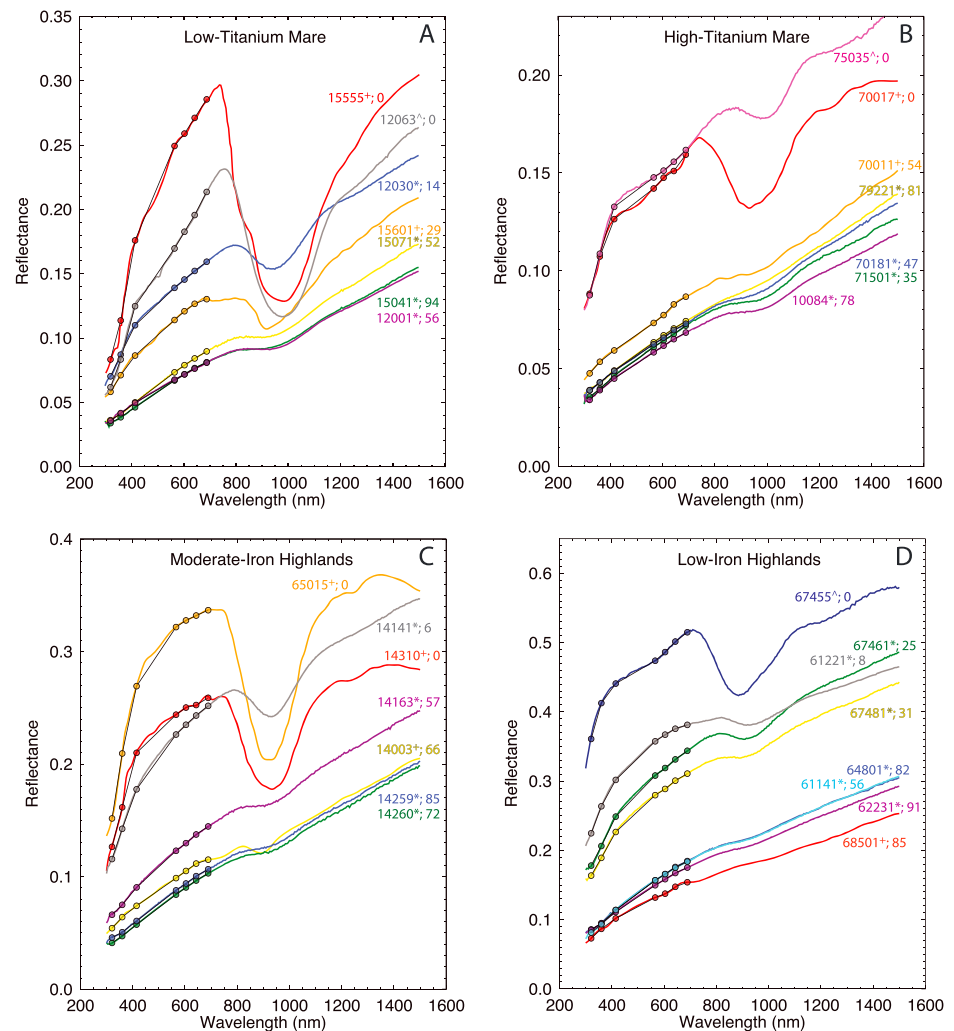


Figure 1. Spectra of soils and powdered rocks from the lunar soil characterization consortium [Taylor *et al.*, 2001, 2010] (indicated with an asterisk), Wagner *et al.* [1987] (indicated with a cross), and RELAB soils (indicated with an inverted open triangle) of varying levels of maturity. Sample number and I_S/FeO value are labeled for each spectrum. The reflectance values convolved to the LROC WAC band passes are shown with circles. The soils are separated into four compositional groups ((a) low-titanium mare, (b) high-titanium mare, (c) moderate-iron highlands, and (d) low-iron highlands) relevant to regions observed with the LROC WAC. Note the different y axis range of each panel.

comparison to observations from the LROC WAC. We separate the samples into four compositional groups: Low-titanium mare soils (2–3 wt % TiO_2 ; Apollo 12 and 15), high-titanium mare soils (7–10 wt % TiO_2 ; Apollo 11 and 17), moderate-iron highland soils (8–10 wt % FeO ; largely Apollo 14), and low-iron highland soils (3–5 wt % FeO ; Apollo 16) (Figure 1). From the LSCC soils, we exclude 71061 because of the high concentration of pyroclastic black beads in this sample, whose spectral properties are dissimilar to typical high-titanium mare soils [Pieters *et al.*, 2000b]. Spectra from Wagner *et al.* [1987] and two spectra from RELAB (67455.63 and 75035.207) of powdered rocks are added to supplement our survey of unweathered soils. One Apollo 16 sample from Wagner *et al.* [1987], 65015, is included with the moderate-iron highland samples as it has an FeO content of ~8 wt % [Haskin *et al.*, 1973]. The spectra shown for the LSCC samples are those of the <45 μm size fraction. The spectra from Wagner *et al.* [1987] were sieved to particles <150 μm , and those from RELAB were bulk (not sieved; 67453.63 and 75035.207). While comparisons among inconsistent particle size fractions are not ideal, we examined other size fractions for the LSCC soils and found no significant variation in 321/415 nm ratio with particle size.

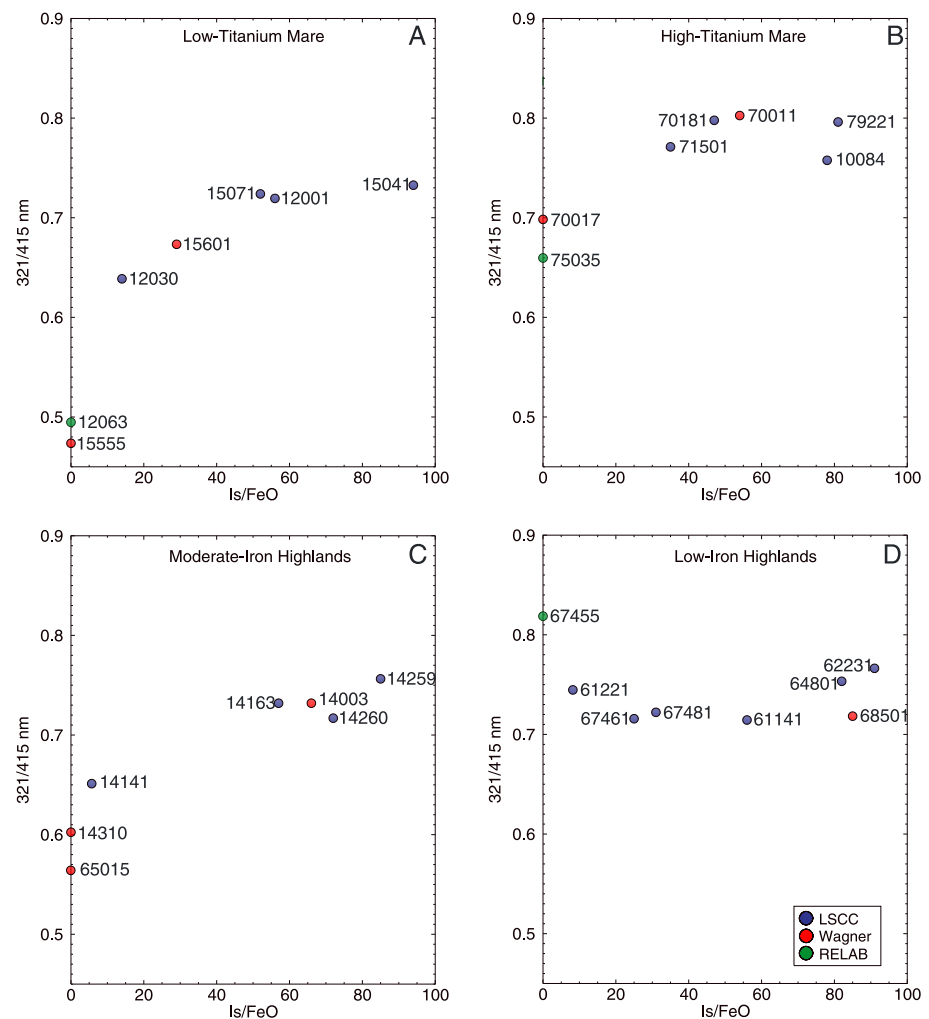


Figure 2. The 321/415 nm ratio values of the soils shown in Figure 1, as compared with their I_s/FeO values.

Spectra for each of the four compositional groups are shown in Figure 1 along with the reflectance values convolved to the LROC WAC filters. Figure 2 shows the corresponding 321/415 nm ratio and I_s/FeO values for each sample. Consistent with previous work [Hendrix and Vilas, 2006], the UV slope is found to decrease (321/415 nm ratio increases) with increasing maturity for the mare and moderate-iron highland samples (Figures 2a–2c). However, this trend is only apparent below I_s/FeO values of ~40; above 40 little to no change in ratio is observed (for reference, soils with I_s/FeO values below 30 are considered immature, 30–60 are submature, and >60 are mature [Morris, 1976]). For low-iron highland samples (Figure 2d), the 321/415 nm ratio is nearly invariant relative to maturity. Among the LSCC samples, the 321/415 nm ratios show little change over an I_s/FeO range of eight to 91. The RELAB spectrum of the “unweathered” sample 67455.63, an anorthositic breccia from North Ray crater with 4–5 wt % FeO [Lindstrom et al., 1977], has a 321/415 nm ratio value that is higher (7%) than the more mature soil samples. These results suggest that as opposed to soils containing more than ~5 wt % FeO, the 321/415 nm ratio of low-iron soils may not change with increased exposure to space weathering processes or may actually decrease. However, characterizing these variations with a broader suite of immature low- to moderate-Fe highland soils will provide better constraints on the UV reflectance properties of space weathering in the highlands in particular, and additional samples of all compositions would help refine the trends now inferred from a relatively small number of samples.

While the mare and moderate-Fe highlands show no marked variation in UV slope for areas with I_s/FeO values above ~40, OMAT values decrease up to I_s/FeO values of ~60 [Lucy et al., 2000a]. This lack of variation in UV slope at $I_s/FeO \gtrsim 40$ may be consistent with only more recently exposed soils retaining a

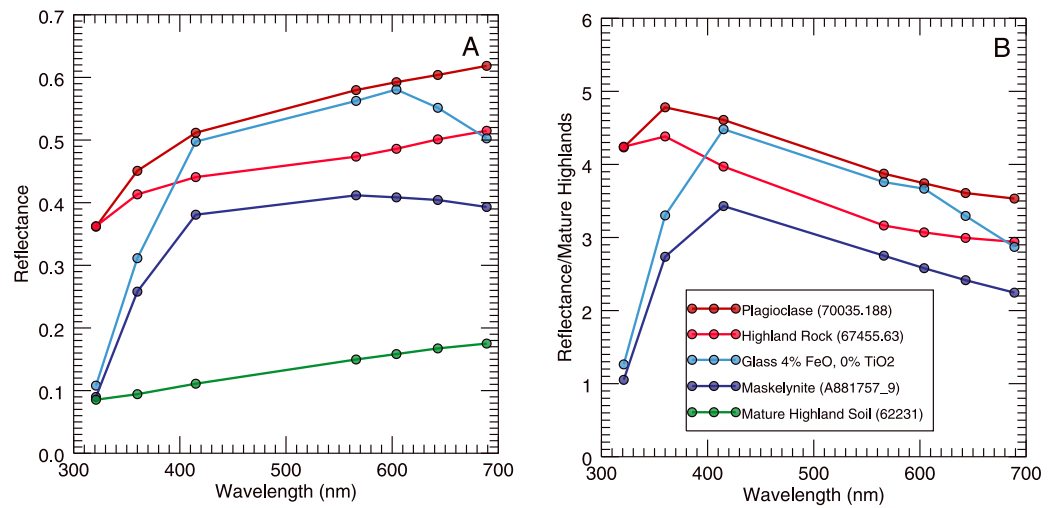


Figure 3. Spectra of materials relevant to the low-iron highlands. (a) Plagioclase separates from sample 70035 [Isaacson *et al.*, 2011], maskelynite [Pieters, 1996], highland-composition glass [Wells, 1977; Blewett *et al.*, 2011b], powdered anorthosite 70035, and a mature highland soil 62231 [Taylor *et al.*, 2010]. (b) Samples shown relative to the spectrum of mature highland soil 62231. Plagioclase shows a break in slope at 360 nm, whereas glass and maskelynite have a steep positive slope below 415 nm.

signature of immaturity in the UV as compared to that in the visible to near infrared (i.e., UV maturity “saturates” earlier), indicating characterization of UV slopes may help pinpoint the “freshest” materials on a surface. These suggestions are evaluated with WAC data in section 3.3.

3.2. The UV Reflectance of Glass

Shock pressures created by hypervelocity impact events can reach > 100 GPa [see Roddy *et al.*, 1977], resulting in a range of effects from simple fracturing of material to melting and vaporization of target rock. Some portion of impact-produced melt may quench to form a glass. Relatively modest shock pressures (~ 25 GPa) can also result in the solid-state transformation of plagioclase to a diaplectic glass known as maskelynite [Milton and de Carli, 1963]. Glasses of lunar composition are absorbing at ultraviolet wavelengths [Wells and Hapke, 1977], and thus their spectral properties are relevant to our study of material associated with fresh impact craters. We note that these glasses are distinct from agglutinitic glasses, whose volumes contain SMFe, which strongly affects their spectral properties.

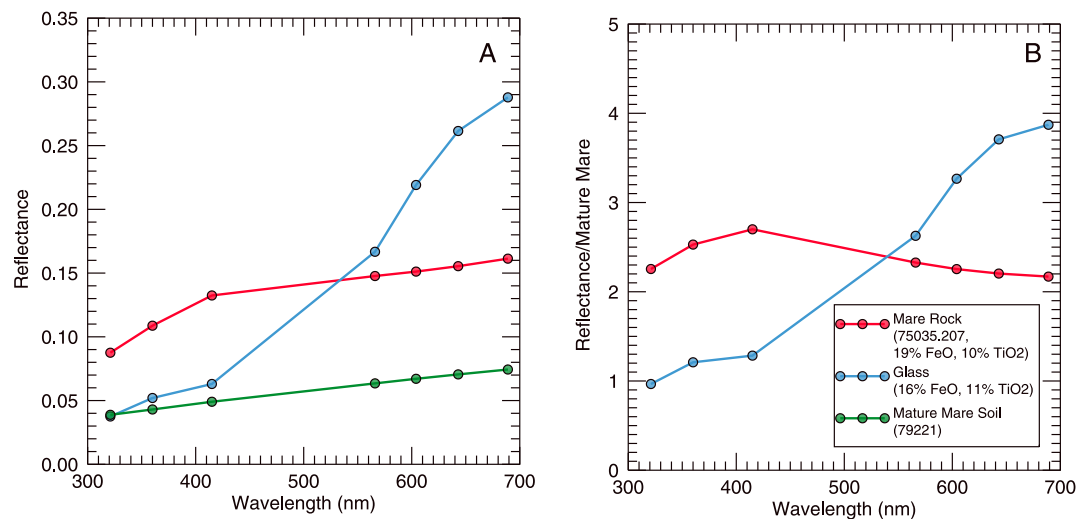


Figure 4. (a) Reflectance of the powdered high-titanium mare rock 75035, mature mare soil 79221, and high-titanium glass [Wells, 1977; Blewett *et al.*, 2011b] of similar composition. (b) Rock and glass shown relative to mature soil 79221. While each has a similar slope < 415 nm, the longer wavelength portions of the spectra are distinct.

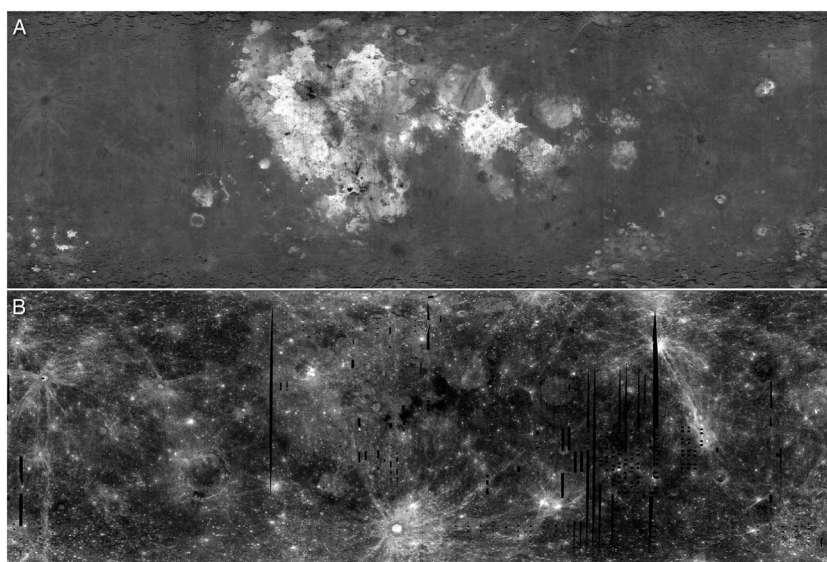


Figure 5. (a) Global (-180° to 180° longitude, $\pm 60^{\circ}$ latitude) view of the 321/415 nm LROC WAC ratio (stretched from 0.66–0.81). (b) OMAT as described by Lucey *et al.* [2000a] (values stretched from 0.1 to 0.3).

In addition to exhibiting lower overall reflectance [Johnson and Hörz, 2003], a comparison between plagioclase, maskelynite, and a synthetic iron-poor glass (Figure 3) shows the glass form is more strongly absorbing in the UV at WAC wavelengths than the crystalline form. The maskelynite and glass samples exhibit a strong downturn

in reflectance at 415 nm, whereas plagioclase displays a decrease in reflectance at wavelengths below 360 nm (Figure 3b). These spectra suggest the 321/360 nm ratio may also provide substantial information for highland compositions and differences in the 321/360 versus 321/415 nm ratios could help distinguish between fresh crystalline plagioclase versus shocked or melted (maskelynite or quenched glass) plagioclase at highland craters.

For iron- and titanium-rich compositions, the effects of glass appear to have a smaller effect on the UV slope (Figure 4) and show only small differences in 321/415 nm ratio. However, the overall shape of the spectrum is distinct for each, allowing discrimination between immature rock and glass in lunar soils.

3.3. Maturity From Global LROC WAC UV Data

In the broad view, it is composition and not maturity that dominates differences in the 321/415 nm ratio WAC mosaic (Figure 5a). Compared to an OMAT parameter image created from Clementine images (Figure 5b), variations due to maturity are subtle; many regions that show high OMAT values show little to no corresponding anomaly in

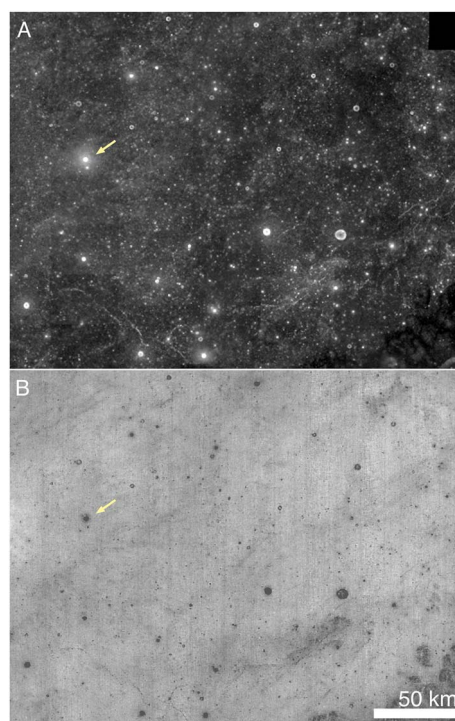


Figure 6. A comparison of (a) OMAT and (b) WAC 321/415 nm ratio in Mare Crisium (scene centered at 14.7°N , 59.1°E). Many small craters with high OMAT values (immature) show smaller or no corresponding decrease in 321/415 nm ratio. For example, some craters whose ejecta display high OMAT values have a decrease in 321/415 nm ratio that is more limited in extent (yellow arrow). Images are stretched to the same values as in Figure 5.

Table 1. Properties of Selected Fresh Craters

Type	Location #	Latitude (°)	Longitude (°E)	Lunar Prospector FeO	Clementine TiO ₂	321/415 Fresh 3 × 3	321/415 nm Fresh Single Pixel	Error	321/415 Mature	Error	% Diff. 3 × 3	% Diff. Single Pixel
Low-Ti mare	1	19.76	24.44	18.0	4.8	0.692	0.688	0.053	0.741	0.050	-6.6	-7.2
Low-Ti mare	2	19.71	22.53	17.7	5.4	0.649	0.649	0.100	0.741	0.025	-12.4	-12.1
Low-Ti mare	3	21.17	23.68	17.3	5.3	0.685	0.662	0.216	0.741	0.026	-7.5	-10.7
Low-Ti mare	4	27.79	11.79	18.6	4.2	0.684	0.672	0.029	0.741	0.026	-7.7	-9.3
Low-Ti mare	5	47.80	290.97	17.8	0.9	0.641	0.665	0.053	0.741	0.030	-13.6	-10.3
Low-Ti mare	6	40.83	289.77	15.5	0.9	0.667	0.654	0.062	0.741	0.042	-10.0	-11.7
Low-Ti mare	7	28.55	325.76	18.9	2.9	0.657	0.655	0.016	0.741	0.018	-11.4	-11.6
Low-Ti mare	8	32.07	328.12	19.9	2.9	0.664	0.659	0.051	0.741	0.022	-10.4	-11.1
High-Ti mare	9	9.88	311.66	22.8	10.0	0.701	0.700	0.056	0.790	0.043	-11.3	-11.4
High-Ti mare	10	13.11	24.50	19.0	14.2	0.763	0.770	0.041	0.790	0.041	-3.5	-2.6
High-Ti mare	11	40.09	333.79	20.9	8.8	0.697	0.700	0.070	0.790	0.025	-11.7	-11.4
High-Ti mare	12	10.89	314.47	20.8	10.4	0.738	0.730	0.045	0.790	0.023	-6.6	-7.6
High-Ti mare	13	-4.98	324.79	20.6	8.4	0.701	0.685	0.095	0.790	0.030	-11.3	-13.3
Mod-Fe highland	14	9.29	250.02	5.5	0.4	0.669	0.673	0.013	0.720	0.081	-7.1	-6.6
Mod-Fe highland	15	-41.33	188.29	10.2	0.9	0.680	0.677	0.019	0.720	0.030	-5.6	-5.9
Mod-Fe highland	16	46.60	49.74	9.4	0.5	0.712	0.698	0.025	0.720	0.035	-1.1	-3.1
Mod-Fe highland	17	4.50	101.06	6.8	0.5	0.696	0.702	0.057	0.720	0.052	-3.4	-2.5
Mod-Fe highland	18	-19.33	302.75	8.1	1.2	0.678	0.675	0.025	0.720	0.048	-5.8	-6.3
Low-Fe highland	19	3.47	259.63	5.1	0.5	0.701	0.692	0.015	0.713	0.074	-1.7	-2.9
Low-Fe highland	20	-5.03	255.58	4.6	0.5	0.677	0.657	0.029	0.713	0.057	-5.0	-7.8
Low-Fe highland	21	7.84	182.96	4.0	0.4	0.707	0.710	0.098	0.713	0.033	-0.8	-0.3
Low-Fe highland	22	17.60	182.00	4.9	0.4	0.706	0.705	0.025	0.713	0.039	-0.9	-1.1
Low-Fe highland	23	19.40	166.69	4.7	0.3	0.696	0.696	0.057	0.713	0.033	-2.3	-2.4
Low-Fe highland	24	18.32	202.68	4.8	0.7	0.727	0.736	0.159	0.713	0.045	2.0	3.3

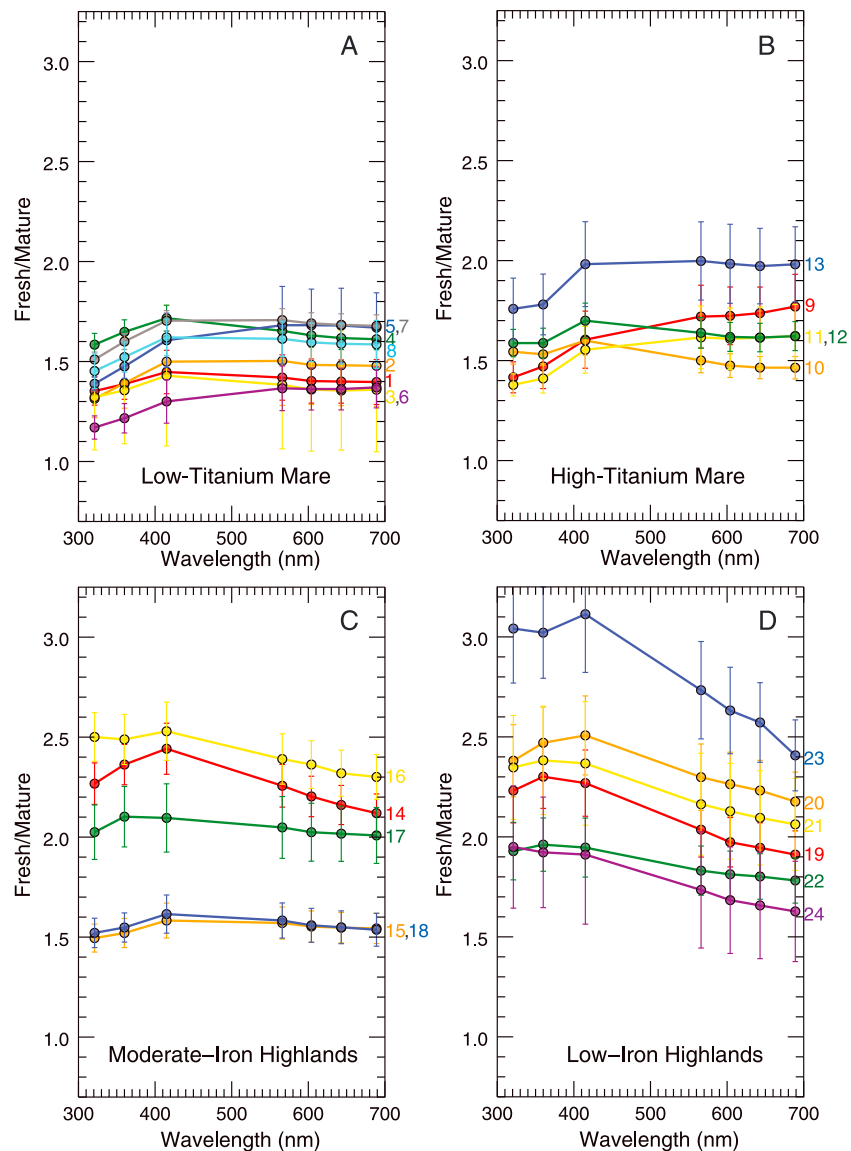


Figure 7. LROC WAC spectra of the fresh craters listed in Table 1 (labels correspond to location numbers given in Table 1). Each spectrum within a compositional group is shown relative to mature material of the same composition to highlight variations due to maturity. The mature spectra were located at 32.12°N, 328.65°E for the low-titanium mare; 11.17°N, 314.44°E for the high-titanium mare; 19.64°S, 302.89°E for the moderate-iron highlands; the low-iron highlands region is located at 27.12°N, 169.81°E and is the same mature standard area used for all subsequent highlands spectra. For the (a) low-titanium mare, (b) high-titanium mare, and (c) moderate-iron highlands, each spectrum shows a break downturn shortward of 415 nm, consistent with laboratory spectra. This region of the spectrum is more variable for the (d) low-iron highlands.

321/415 nm ratio (rays of most large Copernican craters are not easily distinguished from background mature material). However, at a more local scale, variations due to maturity emerge. Small craters (<~5 km) in the mare display low 321/415 nm ratio values, and the rays and near-field ejecta of many small craters also have low ratio values (Figure 6). Small craters are likely to be younger [e.g., Trask, 1971], thus we selected immature craters based on their morphology in NAC images, extensive high-reflectance ejecta blankets, and high OMAT values. The craters were grouped based on their composition to correspond to the four compositional groups of the laboratory spectra using regional FeO values derived from Lunar Prospector data [Lawrence *et al.*, 2002] and estimates of TiO₂ from an

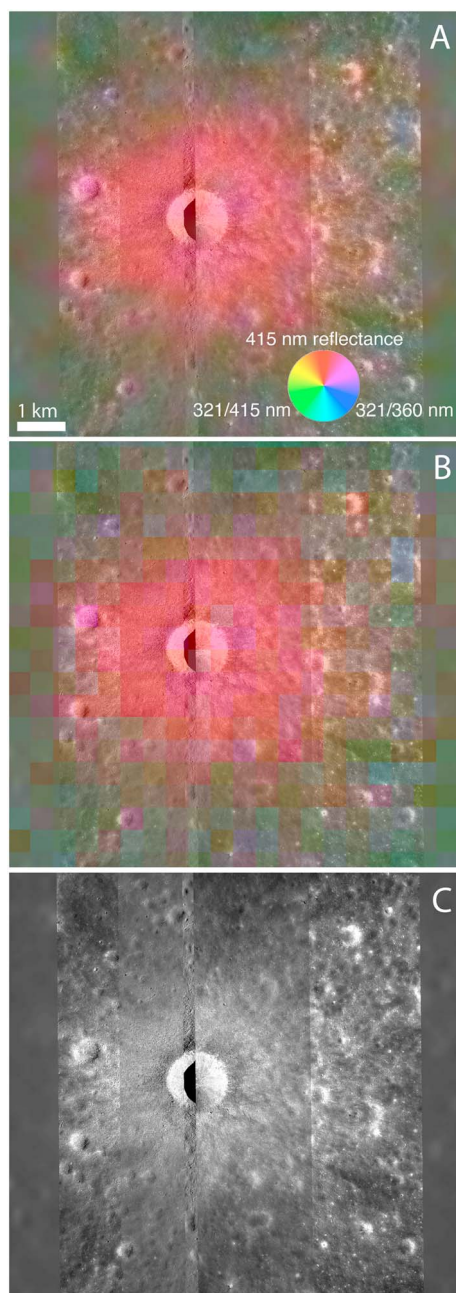


Figure 8. An unnamed crater in Mare Serenitatis (19.716°N, 24.431°E). (a) WAC color overlaid on an LROC NAC image mosaic; WAC image has been resampled using a bilinear interpolation. Color is 415 nm reflectance in red, 321/415 nm ratio in green, and 321/360 nm in blue, and was stretched to highlight variations around the region (0.020–0.035, 0.69–0.78, and 0.83–0.88). (b) The same scene, but nearest neighbor resampling provides an example of the true size of the LROC WAC pixels in relation to the NAC data. (c) LROC NAC mosaic of the mare crater alone. The low-ratio values of this mare crater are associated with the continuous ejecta blanket, and increase with increasing distance from the crater. NAC images M122048260, M175117836, and M146824496.

empirical model using Clementine reflectance [Lucey *et al.*, 2000b]. Selected examples are presented in Table 1 and Figure 7. We collected spectra located on the high-reflectance continuous ejecta deposit of each crater, both by averaging a 3×3 pixel sample, and by taking the value at a single pixel (recall that the mosaic is resampled to a pixel scale larger than its native pixel scale and is the median of 21 near-global mosaics). The uncertainties for the 3×3 box are reported as the standard deviation of the value within that box. For the single pixel, the uncertainty is reported as the standard deviation of all WAC observations of that location. Errors of a ratio are calculated as $DX/X = \{(DA/A)^2 + (DB/B)^2\}^{0.5}$, where $X = A/B$ and the errors of X , A , and B are DX , DA , and DB . The single pixel value may provide a more “pure” sample of the fresh ejecta for small (< 5 km) craters, as a 3×3 box may include some terrain off of the continuous ejecta deposit. Both values are reported in Table 1, and in practice they show little difference. We discuss the values for the 3×3 averages below. Mature spectra were collected for comparison; the same mature area was used for all craters within a compositional group. The mature spectra were located at 32.12°N, 328.65°E for the low-titanium mare; 11.17°N, 314.44°E for the high-titanium mare; and 19.64°S, 302.89°E for the moderate-iron highlands. Low-iron highland spectra here and in all subsequent figures are shown relative to a standard area at 27.12°N, 169.81°E.

Fresh craters in the mare and in moderate-iron highland regions have a steeper UV slope, as seen when their spectra are shown relative to the spectra of mature material (Figures 7a–7c). The spectral properties are generally similar to those of the laboratory spectra, with some exceptions (Table 1). The mare and moderate-iron highlands craters display low 321/415 nm ratios, though none reach the extremes shown for the immature end-member laboratory spectra, whose ratio values are shown in Figure 3. Instead, the fresh crater ratios are generally consistent with values expected for soils with I_0/FeO values of ~ 10 –30. The mature ratio values extracted from LROC WAC data

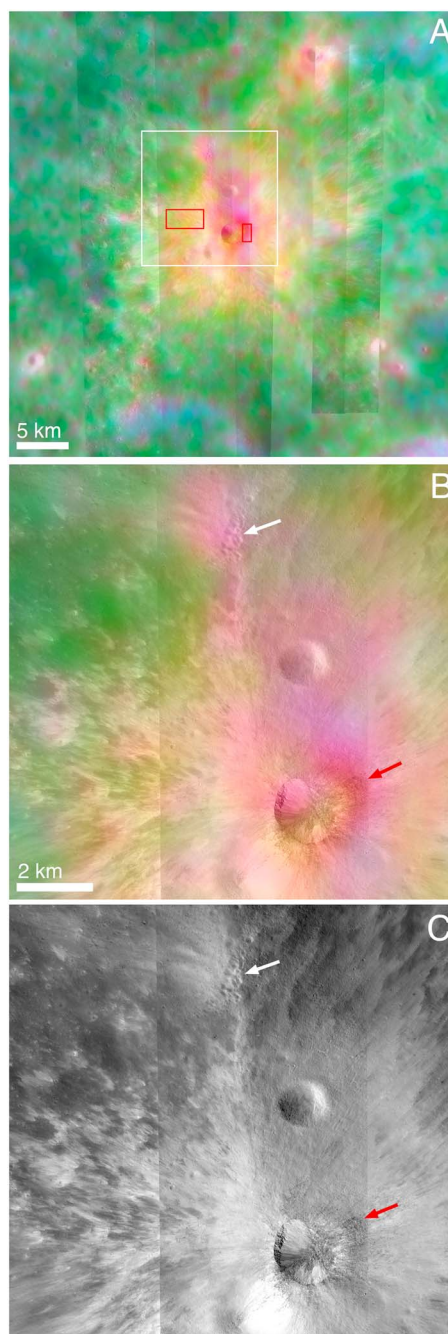


Figure 9. A small highland crater near Zernike W (19.377°N, 166.634°E). (a) Context view of the crater, with the same color scheme as in Figure 8 and described in Table 2, but with a different stretch (0.033–0.075, 0.68–0.75, 0.80–0.89 for red, green, and blue, respectively). This standard stretch is the same for all figures using this color scheme that follows. White box shows the location of Figures 9b and 9c, and red boxes show the locations of spectra displayed in Figure 10. (b) Low 321/415 nm ratio values (red-pink) are observed close to the crater and in regions of impact melt (red arrow), as well as associated with secondary craters (white arrow). (c) Crater shown without color overlay. NAC images M1097758406, M112862170, M121118602, and M184797712. In this color scheme, yellow regions are consistent with relatively fresh, crystalline plagioclase, pink-red regions are consistent with maskelynite or highland-composition glass, and green regions are consistent with mature highlands (Table 2).

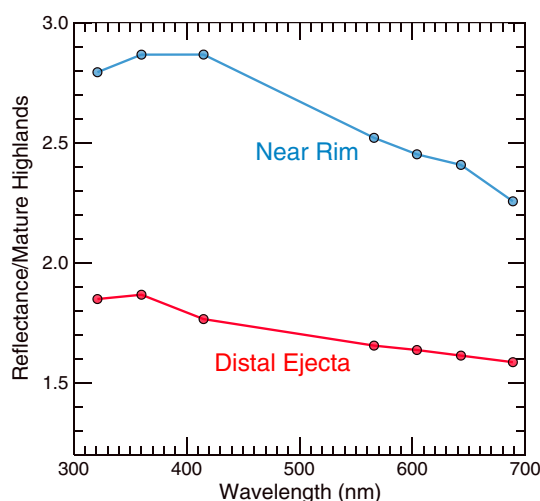


Figure 10. Spectra of the fresh highland crater in Figure 9 shown relative to the same mature highland standard region (27.12°N, 169.81°E); locations of fresh spectra shown in Figure 9a. The near-rim spectrum displays the characteristic downturn shortward of 415 nm, observed for glass and maskelynite in Figure 3b. This region appears to be associated with ejected impact melt (Figure 9c). The more distal ejecta have a shallower spectral slope than the mature highlands, and a small relative downturn at 360 nm rather than 415 nm.

are in agreement with the mature laboratory samples of like composition.

The low-iron highland craters, however, show substantial variation, with 321/415 nm ratio values both above and below those of mature soil. This variation is both larger than that of the other compositional groups and larger than our (limited) laboratory samples indicate. With ratio values both above and below those for mature samples, this wide range suggests that either the laboratory spectra do not capture the range of variations due to maturity or that another factor, such as shock, is affecting freshly exposed material at these craters. This suggestion is assessed in the following section.

3.4. Details of Crater Ejecta Blankets

While the spectra presented above were collected from a small portion of each crater's ejecta, substantial variation is observed within the ejecta blankets of even some small craters. We examine

WAC color images overlaid on NAC images of fresh craters to investigate this local variability. We also focus on the differences between high-reflectance, fragmental ejecta and regions of now-frozen impact melt. Impact melt deposits may have a substantial glass component [e.g., Schaber *et al.*, 1972; Wilshire and Moore, 1974], and because glass can also have strong UV absorption features (section 3.2), we explore the contribution of glass to the observed spectral differences at fresh craters. To do so, we use a red-green-blue composite in which 415 nm reflectance is shown in red, 321/415 nm ratio is shown in green, and the 321/360 nm ratio is in blue. Expected composite colors for various materials, based on laboratory spectra, are shown in Table 2.

The large spatial resolution difference (~800X) between the WAC and NAC data sets poses challenges. We thus resample the WAC data to higher resolution using both bilinear interpolation and nearest-neighbor sampling and examine each in all cases. We look at the smaller craters described above and selected large Copernican craters, including Giordano Bruno, Tycho, Necho, and Jackson.

3.4.1. Small Craters

Small (≤ 5 km), fresh craters in the lunar maria generally have a steep slope throughout the UV and thus have low 321/360 and 321/415 nm ratio values within ~1 crater diameter, corresponding to the high-reflectance continuous ejecta deposit (Figure 8). Beyond the continuous ejecta, the UV ratios fade to background, mature mare levels. No clear difference in these ratios is observed for impact melt, when it is resolved, as compared to the high-reflectance, fragmental materials.

Relative to mare craters, small highland craters often show more complex relationships within their ejecta. In many cases, the regions closest to the crater (≤ 1 crater diameter from rim) show lower

Table 2. UV Spectral Properties of Fresh Material, Relative to Mature Material of Same Composition

	415 nm Red	321/415 nm Green	321/360 nm Blue	Composite Color
Iron-rich	High	Low	Low	Red
Highland crystalline	High	High	Moderate	Yellow
Highland shocked/melted	Moderate-High	Low	Moderate-Low	Pink-Red

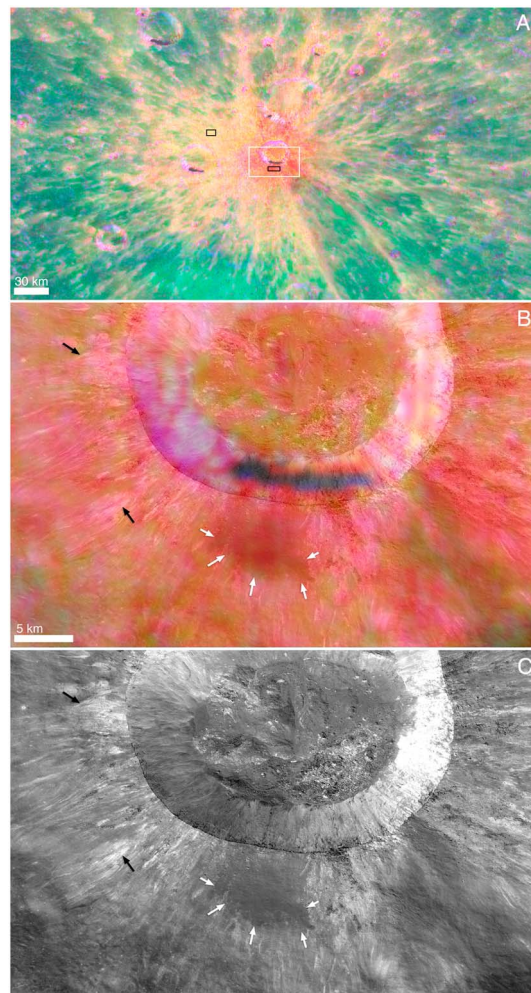


Figure 11. (a) Context view of the WAC color composite (Table 2; same stretch as in Figure 9) for Giordano Bruno crater. Low 321/415 nm ratio values are observed close to the crater (pink-red), whereas the more distal ejecta (yellow) has slightly higher ratio values than the mature background (green). The white box indicates the extent of Figures 11b and 11c, and the black boxes show the locations of spectra in Figure 13a. (b) A closer view of the southern portion of Giordano Bruno, shown with the 321/415 nm ratio values overlain on an LROC NAC mosaic (anomalous ratio values are found on the southern crater wall due to persistent shadows in the data). Both impact melt (white arrows) and high-reflectance fragmental ejecta (black arrows) have low 321/415 nm ratio values close to the crater rim. (c) LROC NAC mosaic of Giordano Bruno.

321/415 nm ratio values (e.g., pink and red regions in Figure 9) as compared to nearby mature soils (green). These areas are generally associated with portions of the continuous ejecta blanket. Beyond the continuous ejecta, similar ratio values are often associated with secondary craters. Areas with high 321/415 nm ratios (yellow) typically correspond to the more distal ejecta and rays (Figure 9). In cases where impact melt deposits associated with small highland craters are resolved in the WAC UV mosaic, the 321/415 nm ratio value is generally lower (red, Figure 9) than the mature background. Spectra collected from the low-ratio region associated with impact melt near the crater rim show a break in slope at 415 nm when ratioed to mature highlands; spectra of the high-ratio rays farther from the crater show a break in slope instead at 360 nm (Figure 10) and reflectance values that are intermediate between the near-rim spectra and mature highlands.

3.4.2. Large Craters

Giordano Bruno crater (22 km in diameter) is one of the youngest large impact craters on the Moon, with an estimated age on the order of <10 My based on its crater size–frequency distribution [Morota *et al.*, 2009]. It is also the site of some of the highest reflectance material on the Moon, with blocky, fragmental ejecta and well-preserved flows and ponds of impact melt [Bray *et al.*, 2010; Denevi *et al.*, 2012]. Similar to many small, fresh highland craters (e.g., Figure 9), Giordano Bruno is surrounded by a region of low 321/415 nm ratios, which is mainly limited to the continuous ejecta deposit but also extends along some high-reflectance rays (Figure 11). Within the continuous ejecta deposit, the regions of the lowest 321/415 nm ratio (values of ~ 0.67 – 0.68 , 6%

below mature highlands) correspond to both high-reflectance blocky and fragmental ejecta and regions of solidified impact melt (Figure 11b). Similar to the observations of smaller craters, beyond the low-ratio materials, most of the distal ejecta and rays have 321/415 nm ratio values that are higher than those of mature highlands and similar to lower 321/360 nm ratios (Figure 11). Similar relationships are observed at other highland craters such as Tycho, Jackson, and Necho, which are older than Giordano Bruno (>100 Ma) but still Copernican in age, with one main difference: these craters have a region ≤ 1 crater radius from the rim that is low in 321/415 nm ratio, but also lower in albedo than the crater rays and more distal ejecta (Figure 12). For Tycho, this low-reflectance halo surrounding the crater rim has been interpreted to be the result of a high proportion of impact-produced glass [Smrekar and Pieters, 1985; Hawke *et al.*, 1986], and at Necho, large flows and ponds of impact melt are observed to the northeast and

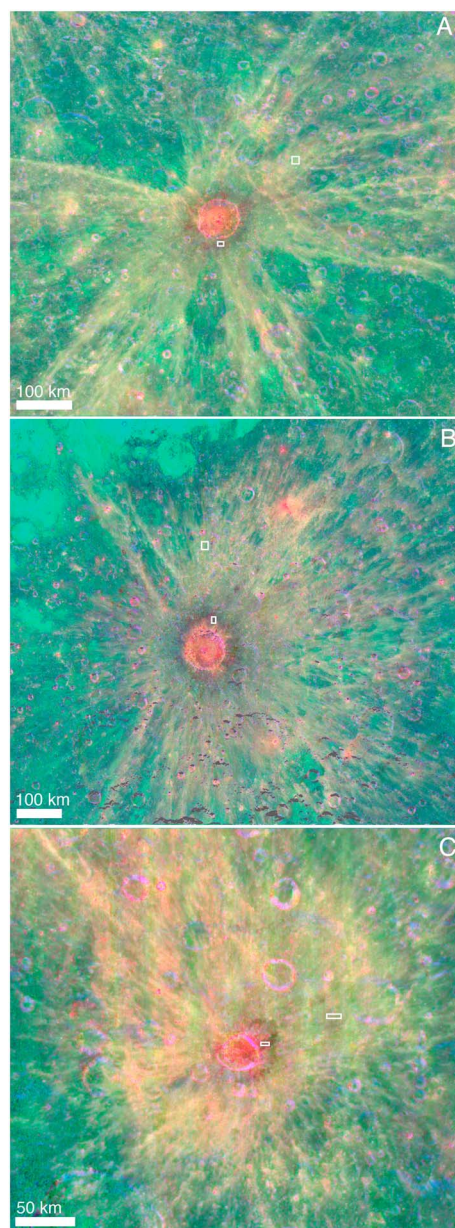


Figure 12. WAC color composite (Table 2) views of (a) Jackson, (b) Tycho, and (c) Necho craters overlaid on an LROC WAC mosaic. The white boxes in each panel show the locations of spectra in Figure 13b.

high-reflectance ray material, with no clear relationship to secondary craters, which is responsible for the high 321/415 nm ratios.

3.5. Lunar Swirls

Lunar swirls are sinuous high-albedo features hundreds of kilometers in extent with no topographic relief that are collocated with crustal magnetic anomalies [e.g., *El-Baz, 1972; Hood et al., 1979; Hood and Williams, 1989*]. Determining their origin has proved enigmatic, and proposals include cometary impact [e.g., *Schultz and Srnka, 1980*], meteoroid swarm [*Starukhina and Shkuratov, 2004*], accumulation of feldspar-rich dust through electrostatic levitation affected by the magnetic anomaly [*Garrick-Bethell et al., 2011*], and atypical space weathering as a result of magnetic shielding from the charged solar wind particles [e.g., *Hood and Schubert, 1980; Hood and Williams, 1989*]. Recent work appears to be

east of the crater [*Hawke and Head, 1977*]. Near the rim of each crater, the 321/415 nm ratio is slightly lower than values for mature highland soils. The high-reflectance rays of each crater have slightly higher 321/415 nm ratios than mature highland soils.

We compare the WAC spectra of these regions of Giordano Bruno, Tycho, and Jackson to laboratory spectra of plagioclase, maskelynite, and low-iron synthetic glass. We show each spectrum relative to mature lunar highlands (standard area at 27.12°N, 169.81°E) to highlight differences in spectra shape. The spectra for the melt-rich region on the southern rim of Giordano Bruno, as well as the impact melt flows east of Necho and the Tycho and Jackson halos all show a break in slope at 415 nm and a larger turn down at 415 nm (Figure 13), consistent with the glass and maskelynite spectra (Figure 3b). The spectra of the rays of each crater show only a slight break in slope at 360 nm (Figure 13), similar to the plagioclase and powdered Apollo 16 rock spectra (Figure 3b). We note that the relative reflectance values for Giordano Bruno are substantially higher for both the ray and melt-rich region (2.0 and 1.9, respectively, at 415 nm) than for the Tycho, Jackson, and Necho rays (~1.4). The Tycho and Jackson halos are only slightly higher in reflectance than mature highlands (~1.1–1.2).

While at the broad scale rays have higher 321/415 nm ratio values than their surroundings, the details are more complex. Within the rays we observe small regions of low 321/415 nm ratio, with values similar to those observed proximal to the crater rim. When compared with NAC images, these low-ratio regions are observed to occur in association with secondary craters within the ray (Figure 14). It is the surrounding

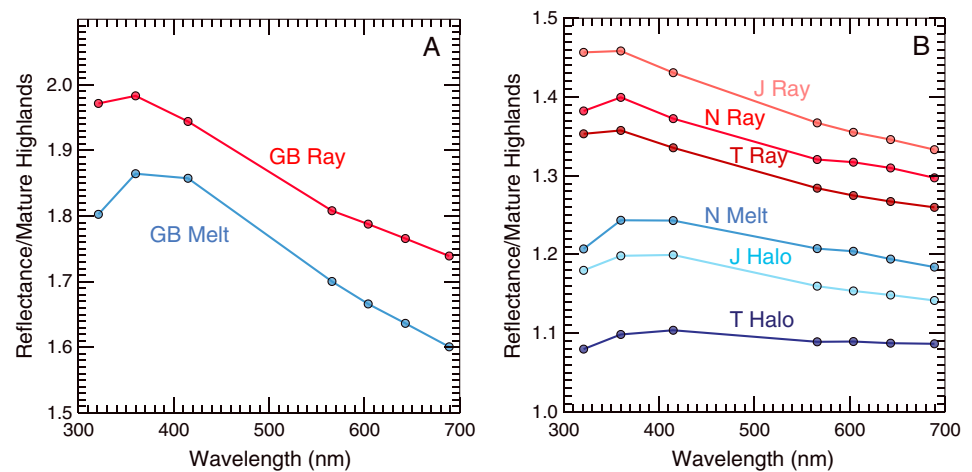


Figure 13. (a) Spectra of Giordano Bruno (GB) crater from the locations in Figure 11. (b) Spectra of Tycho (T), Necho (N), and Jackson (J) craters from the locations in Figure 12. The rays of each crater display a break in slope at 360 nm consistent with crystalline plagioclase-rich soil (Figure 3b). The melt-rich regions of Giordano Bruno and Necho, and the low-reflectance halos of Jackson and Tycho craters show a turndown at 415 nm, consistent with either maskelynite or impact glass (Figure 3b) produced by impact shock. Note the different y axes of Figures 13a and 13b, with the Giordano Bruno ray and melt being substantially higher in reflectance than materials at the other craters. All spectra are shown relative to our mature highland standard region (27.12°N, 169.81°E).

leading to a consensus around the solar wind shielding hypothesis, with direct observations of the deflection of the solar wind at swirls associated with magnetic anomalies [e.g., Wieser *et al.*, 2010; Lue *et al.*, 2011], shallower visible-near-infrared slopes for soils within swirls [e.g., Blewett *et al.*, 2011a; Kramer *et al.*, 2011] and weaker 2.8 μm absorptions indicative of reduced formation of hydroxyl due to solar wind interactions [Kramer *et al.*, 2011].

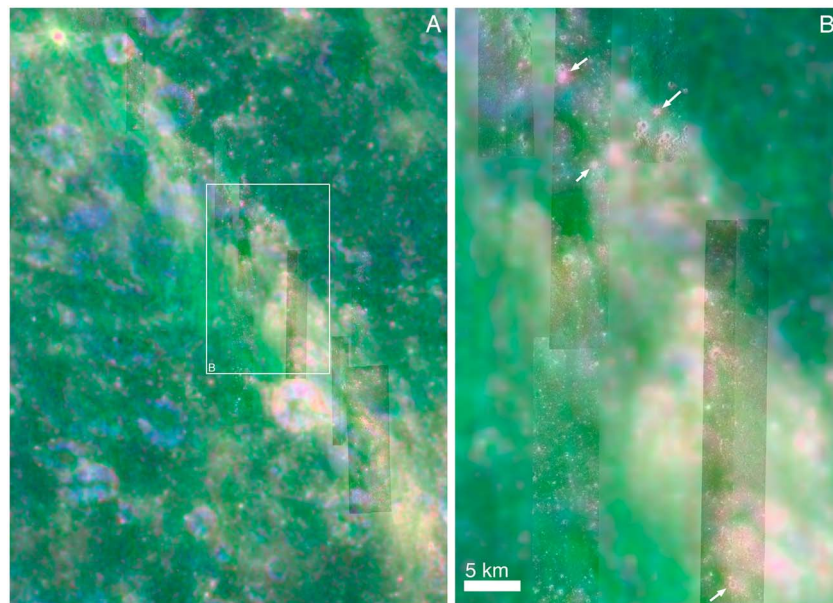


Figure 14. WAC color composite overlay on NAC and WAC mosaic of a ray of Jackson crater (10.462°N, 203.229°E). Within the ray, secondary craters (a few of which are indicated with white arrows) have low 321/415 nm ratios (pink), whereas other portions of the ray (yellow) have a high ratio in comparison with mature highlands (green). NAC images M158619312, M127959440, M110261760, M107904503, and M107897744.

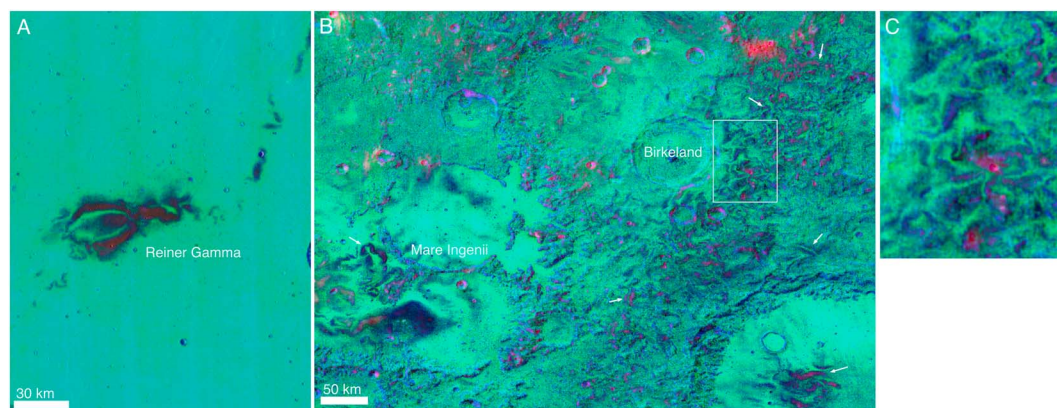


Figure 15. WAC color composite for (a) Reiner Gamma and the (b, c) Mare Ingenii region. The 321/415 nm and 321/360 nm ratio values are low for the swirls. For consistency, these are shown with the same standard stretch as for previous highland figures, despite these being moderate- to high-iron regions with lower overall reflectance (and thus lower values in the red channel). (c) The intricate loops of the Ingenii-region swirl continue into the region east of Birkeland crater.

While impact craters excavate fresh material from depth, which is then exposed to space weathering via the solar wind and micrometeorite bombardment, space weathering at lunar swirls may be predominately the result of micrometeorite bombardment. Thus LROC WAC observations of swirls provide a valuable comparison to our observations of the effects of space weathering at impact craters.

Swirls in moderate- to high-iron regions exhibit low 321/415 nm ratio values (Figure 15) and in fact appear to have larger extents than previously recognized in some cases, such as the swirls in the Mare Ingenii region. We examine three of the swirls associated with “strong” magnetic anomalies as classified by *Blewett et al.* [2011a] (magnetic anomaly strengths of 20–28 nT): Reiner Gamma, Ingenii, and Gerasimovich. We also include the Mare Marginis swirl, which covers both a low-titanium mare as well as moderate-iron highlands. The Marginis swirl is listed as having a “weak” magnetic anomaly with the caveat that coverage of this region by the Lunar Prospector magnetometer was poor [Blewett et al., 2011a].

Reiner Gamma is located in Oceanus Procellarum in a region of high titanium (7–9 wt % TiO_2). Within the high-albedo region of Reiner Gamma, low 321/415 nm ratio values (down to 0.65) are observed, similar to the ratios of unweathered laboratory samples (Figure 2b) and substantially lower than the 321/415 nm ratios (0.71–0.77) of nearby fresh impact craters (Figure 16). The Reiner Gamma ratio values are also lower than those of the fresh craters we examined in all regions of high-titanium mare (Figure 7 and Table 1). WAC spectra shown relative to nearby mature material show that for a profile across a portion of Reiner Gamma, the steep UV slopes rapidly shallow away from the swirl, and the ejecta of nearby fresh impact craters have spectral slopes and overall reflectance values similar to those observed near the margin of the swirl (Figure 16).

The low 321/415 nm ratio values (steep UV slope) at Reiner Gamma could be due to the exposure of fresh mare basalt (reduced or atypical space weathering). Alternately, the low ratio could indicate the presence of titanium-rich glass resulting from the vitrification of mare basalt due to micrometeorite bombardment without the additional SMFe produced by the solar wind. We discriminate between these two scenarios by comparing the Reiner Gamma WAC spectra (Figure 16), shown relative to nearby mature mare basalt, to laboratory spectra of powdered high-titanium basalt and to high-titanium, high-iron glass (Figure 4). The Reiner Gamma spectra closely match the titanium-rich basalt sample, with a strong downturn below 415 nm and the absence of the characteristic steep positive slope at wavelengths greater than 415 nm observed for the glass. Thus we conclude that the low 321/415 nm ratio values at Reiner Gamma are mainly due to mare basalt that has experienced low levels of space weathering from the solar wind.

Similar relationships are observed for the Ingenii and Marginis swirls within the mare and moderate-iron highlands such as those of the South Pole-Aitken basin, with low 321/415 nm ratios (Figure 15) as compared

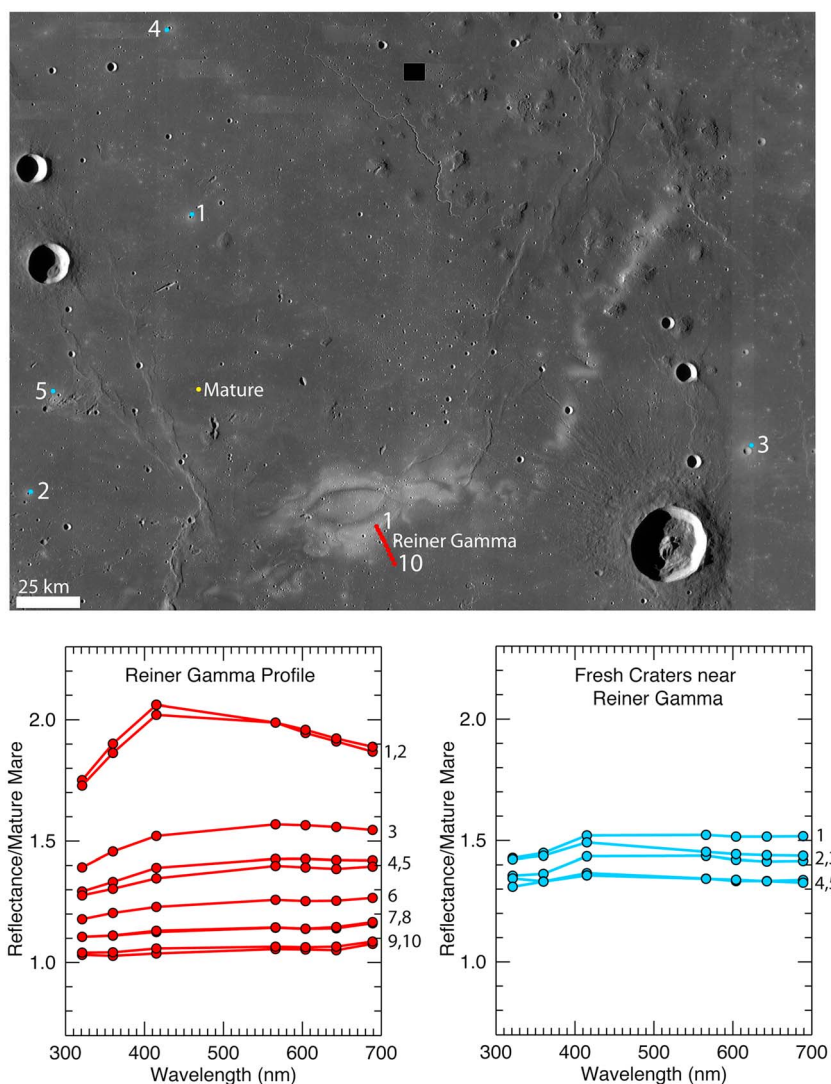


Figure 16. (top) WAC monochrome mosaic (643 nm) of a portion of the Reiner Gamma swirl. (bottom left) WAC reflectance spectra for a profile across Reiner Gamma (locations of spectra shown at top with red dots), shown relative to local mature material (yellow dot). (bottom right) Spectra for fresh craters (numbered blue dots in the context image) shown relative to same local mature material.

to nearby fresh craters. For the Gerasimovich swirl, located in low-iron (<5 wt % FeO) highlands, we find that regions within the swirl have higher 321/415 nm ratio values than the mature background and low 321/360 nm ratios (yellow, Figure 17). The 321/415 nm ratio values for the Gerasimovich swirl are similar to those of the rays of Tycho, Jackson, and Necho (0.72).

4. Discussion

4.1. The Effects of Space Weathering at Ultraviolet Wavelengths

The spectra of fresh craters in the mare and moderate-iron highlands match laboratory results which show that the strong ultraviolet slope at wavelengths below 415 nm is reduced with increasing exposure to space weathering. The ejecta blankets of fresh craters in these moderate- to high-iron regions show an orderly transition from the lowest 321/415 nm ratios closest to the crater to higher ratios that fade to background mature values beyond the continuous ejecta deposit. The wavelengths of the LROC WAC are well suited for distinguishing between the diagnostic spectral features of glasses and typical lunar rock-forming minerals (Figures 3 and 4). While impact-produced glass is surely present in some abundance at fresh impact craters,

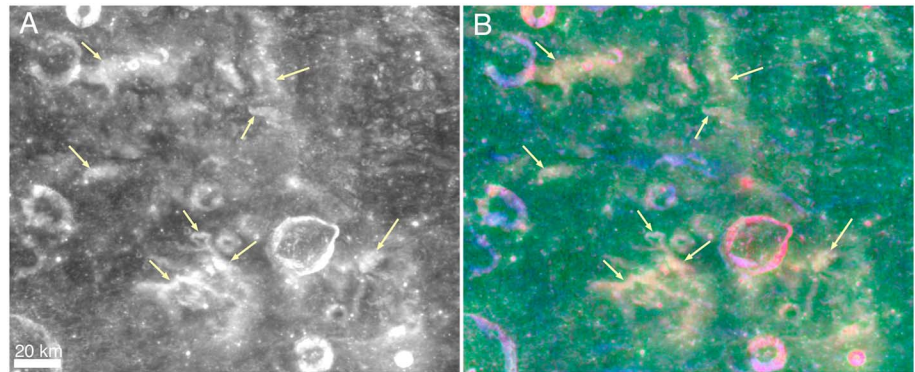


Figure 17. WAC reflectance and color composite of the Gerasimovich swirl, located in a highland region with <5 wt % FeO (21.55°S , 236.92°E). Similar to the distal rays of highland craters, the swirl has slightly higher 321/415 nm ratio values consistent with the exposure of fresh plagioclase-rich soil.

for these moderate- to high-iron craters, the spectral effects of exposed fresh rock dominate, and glass associated with impact melt appears to be only a secondary control on reflectance.

However, in the low-iron highlands, more complex patterns are observed within the continuous ejecta deposits and distal rays of fresh craters, with the general pattern being that of 321/415 nm ratio values lower than mature highland soils close to the crater ($\lesssim 1$ crater diameter), ratio values higher than mature soil within the more distal ejecta, and then a return to the average mature background (e.g., Figure 9). We interpret the low ratio values close to the crater as being due to the presence of maskelynite, transformed from plagioclase as a consequence of shock pressures from the impact event. The spectral shapes, with a downturn at 415 nm (Figure 10), of the proximal ejecta of these highland craters are consistent with either maskelynite or a low-iron, low-titanium glass, and both are likely present. However, the observations presented here for more iron-rich crater deposits indicate that the volume of impact glass produced during impact events is generally not sufficient to dominate the spectral properties. A key difference for the plagioclase-dominated highlands may be the lower shock pressures required to transform plagioclase to its glass equivalent, maskelynite. Thus, at highland craters, our observations are consistent with transitions between regions that experienced different levels of shock. For small craters (e.g., Figure 9), the fact that higher 321/415 nm ratios and a downturn at 360 nm (Figure 10), consistent with the exposure of crystalline plagioclase (lower degrees of shock), are observed farther from the crater may indicate that much of this material is locally disturbed fresh soil rather than primary ejecta. This same phenomenon is seen for the rays of large craters. Secondary craters within rays have low 321/415 nm ratios, consistent with higher degrees of shock, but the surrounding high-reflectance ray has a high ratio (lower shock) (Figure 12). The high-ratio portion of the ray may thus be due to the emplacement of primary ejecta with lower degrees of shock or a large component of local fresh soil exposed by cratering and debris surges. This second scenario (local material) is consistent with ballistic sedimentation models [e.g., Oberbeck, 1975; Oberbeck *et al.*, 1975] and observations of crater rays [Pieters *et al.*, 1985; Hawke *et al.*, 2004] that suggest a large contribution of local material to crater rays. Resolved ultraviolet measurements of highland craters may help to provide additional constraints on local versus primary ejecta and on the degree of shock that ejecta experienced.

These UV observations are consistent throughout the highlands, where spectral properties consistent with higher degrees of shock or quenched melt are found close to craters, and exposures of fresh crystalline plagioclase are farther from the crater within rays (Figure 18). The distinct differences between the UV properties of crystalline plagioclase and its shocked or melted glass equivalent are consistent with broadening of the <300 nm absorption band due to vitrification. Glasses contain only short-range crystallographic order, and thus their absorption bands are broader in this visible and near-infrared [Bell *et al.*, 1976; Wells and Hapke, 1977]; it is likely that the same happens in the UV. Thus while we are only seeing a small portion of the shoulder of the absorption band of plagioclase, manifested as a small downturn at 360 nm, the disordered glass absorption band is broader and thus we observe more of the band at WAC wavelengths, resulting in a stronger downturn at a slightly longer wavelength (415 nm) (Figure 3).

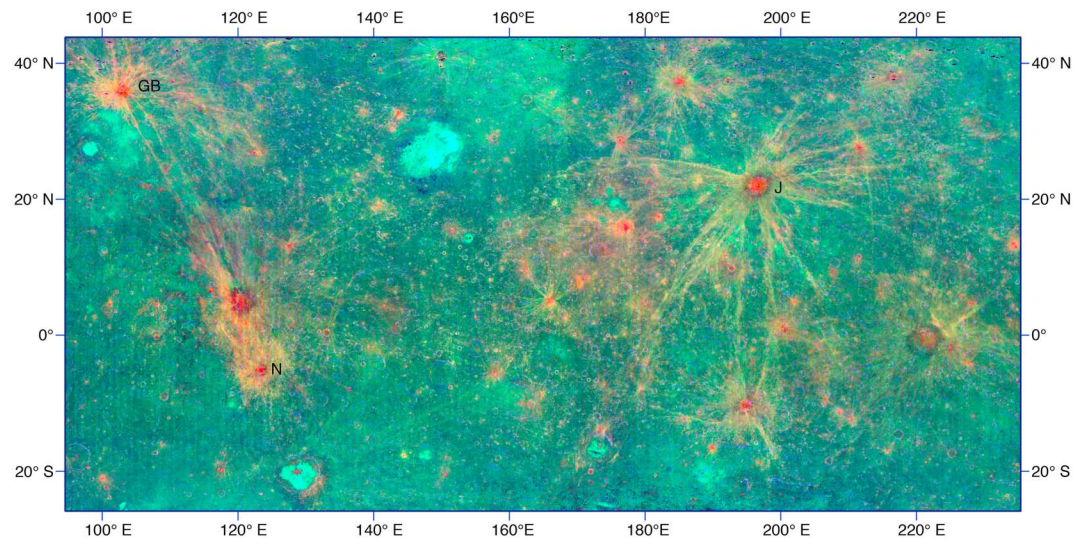


Figure 18. WAC color composite (Table 2) showing a broad region of the highlands. Giordano Bruno (GB), Necho (N), and Jackson (J) craters are indicated.

The spectral properties of the low-reflectance and low-ratio halos (Figure 13b) observed around many large Copernican highland craters (including Tycho, Jackson, and Necho) are also consistent with a large component of impact melt-derived glass, maskelynite, or both. These craters formed >100 Ma and have experienced substantial degrees of space weathering. The comparison with Giordano Bruno, which lacks the low-reflectance halo but does have low UV ratios close to the crater, suggests a weathering progression, where the reflectance of the glass/maskelynite-rich regions decreases more rapidly with exposure on the surface than that of the freshly exposed plagioclase.

4.2. Implications for the Rates and Causes of Space Weathering

Samples with I_s/FeO values beyond ~ 40 show little to no change in their 321/415 nm ratio values, which suggest that spectral changes at ultraviolet wavelengths due to space weathering may “saturate” at slightly lower levels of maturity (I_s/FeO values of 40 are considered submature, with the immature-submature transition at $I_s/\text{FeO} = 30$ [Morris, 1976]) than in visible and near-infrared wavelengths. More spectra of laboratory samples with I_s/FeO values <40 would clarify this relationship. For comparison, OMAT is correlated with I_s/FeO up to values of 50–60 (see Lucey *et al.* [2000a, Figure 2]), where the submature-mature transition occurs at 60.

In this context, the LROC WAC data of small, fresh craters shows that even for these presumably very young craters (~ 50 My based on the age of North Ray crater [Arvidson *et al.*, 1975]), they do not reach the laboratory extremes for fresh material and have 321/415 nm ratio values consistent with I_s/FeO values of 10–40. In other words, in <50 My, fresh materials reach I_s/FeO values consistent with submature soils. However, we do observe ratio values that approach those of “unweathered” laboratory spectra at lunar swirls. Because it appears that swirls occur in regions where magnetic anomalies create “mini magnetospheres” that shield the surface from the solar wind [e.g., Hood and Schubert, 1980; Hood and Williams, 1989], this observation suggests a dominant and fast-acting role of solar wind in the space weathering process, consistent with observations of asteroids [Vernazza *et al.*, 2009]. However, the relatively low spatial resolution of the WAC (pixel scale of 400 m) is a concern for fully characterizing the UV properties of relatively small craters. Though they were carefully selected, even our single pixel spectra may, in some cases, cover a mix of immature ejecta and local mature material. An ultraviolet imager with a spatial resolution that is an order of magnitude higher would enable a finer level of detail for discriminating among the freshest materials on the surface.

It is also important to note that the WAC spectra within swirls like Reiner Gamma have spectral shapes consistent with the exposure of fresh mare basalt (Compare Figures 4b and 16). This observation suggests that the relatively high albedo of swirls is not related to the deposition of plagioclase dust [Garrick-Bethell *et al.*, 2011], as both the spectral shape and UV ratio values are unlike those for either fresh or weathered plagioclase (except when swirls are located in the low-iron highlands). The spectral shapes also indicate

impact melt-produced glass is a relatively minor contributor to the low 321/415 nm ratios of swirls. The lack of a spectral signature of voluminous impact melt glass indicates micrometeorite bombardment may be more effective at exposing fresh material via comminution or excavation than it is at vitrifying soil components. Unless swirls are relatively young features, micrometeorite bombardment, in the absence of the solar wind, is not an efficient agent of maturation.

Extending studies of maturation procession in this wavelength range (~300–700 nm) to other bodies such as Mercury and asteroids will likely further elucidate the relative roles of solar wind processes versus impact bombardment. For Mercury, the likely extreme space weathering environment [e.g., Cintala, 1992] suggests that variations in UV slope due to maturity should persist for a relatively shorter time than on the Moon, and spectra of the low-iron surface should be strongly affected by the high degrees of shock that accompany the higher impact velocities. Conversely, for the asteroid belt, the relatively smaller effects of the solar wind and lower impact velocities should result in more variation in UV slopes at fresh craters due to the longer preservation before homogenization due to space weathering (though a more mobile regolith on small bodies may counteract this trend).

5. Conclusions

Laboratory spectra examined in this study and in previous work [Hendrix and Vilas, 2006] are consistent with a shallowing of UV slope at wavelengths shorter than ~415 nm due to space weathering for moderate- to high-iron compositions. Low-iron highland samples show less variation with maturity but suggest that higher 321/415 nm ratio values may be expected for the most immature samples. Thus spectral trends related to space weathering are identified, but they are dependent on composition. The study of additional laboratory samples, especially those with I_g/FeO values below ~40 would greatly benefit a refined understanding of these trends.

LROC WAC ultraviolet-visible observations of fresh impact craters are consistent with the laboratory results for moderate- to high-iron compositions. Low 321/415 nm ratio values indicate a steep UV slope, and spectral shapes are consistent with the exposure of relatively fresh rock. The 321/415 nm ratio values do not reach the lows observed for unweathered laboratory samples and are instead consistent with I_g/FeO values in the range of 10–40.

Low-iron highland craters exhibit more variation in their ejecta, with 321/415 nm ratio values that are lower than mature material close to the crater and higher than mature material within the more distal ejecta. Large rayed craters share these characteristics and within their rays have small regions of low 321/415 nm ratios associated with secondary impact craters and high ratio values for background ray material. Where higher ratios are observed, we interpret these as consistent with the exposure of fresh crystalline plagioclase-rich soil. Where low ratio values are observed, we interpret these to be related to a higher proportion of shocked plagioclase (maskelynite, and likely, to a lesser degree, glass produced by complete melting of the target rock). These interpretations are consistent with a lower degree of shock and/or the exposure of fresh local material in more distal ejecta and rays and can give insight into the relative importance of deposition versus excavation.

The stronger UV downturn at a slightly longer wavelength for maskelynite and glass is likely the result of broadening of the plagioclase UV absorption band due to vitrification, so that more of its wing is observable at WAC wavelengths.

Low UV ratios observed for swirls in the mare and moderate-iron highlands and high ratios for swirls in the low-iron highlands are consistent with the associated magnetic fields shielding the surface from the solar wind and reducing space weathering. Swirls such as Reiner Gamma exhibit substantially lower levels of space weathering than nearby fresh craters, and their spectral shapes are diagnostic of exposed fresh mare basalt rather than impact glass. These observations indicate that micrometeorite bombardment alone is an inefficient agent of space weathering, and while micrometeorite impacts surely result in some degree of vitrification of the soil, the lack of a clear glass signature in the WAC spectra suggests that they may be more effective at comminuting and exposing fresh unweathered surfaces.

The LROC WAC observations reported here show UV reflectance to be a key diagnostic tool for quantifying the state of maturity of the youngest lunar soils. Future remote sensing platforms that include high-resolution

(pixel scales of 50 m or smaller) UV and visible imaging capabilities may allow relative temporal resolution among late Copernican craters, and ultimately absolute ages when enough young ($\lesssim 200$ my) lunar soils are age dated.

Acknowledgments

We thank Carle Pieters, Myriam Lemelin, and an anonymous reviewer for their helpful reviews. This work was supported by the National Aeronautics and Space Administration Lunar Reconnaissance Orbiter Project contract NNG07EK00C. This research utilizes spectra acquired by Carle Pieters with the NASA RELAB facility at Brown University, and makes use of the USGS Integrated Software for Imagers and Spectrometers (ISIS). We wish to thank Kris Becker and Jeff Anderson at the USGS Astrogeology Center in Flagstaff for their support in developing the tools to process and analyze LROC WAC data. LROC data are archived in the Planetary Data System.

References

- Allen, C. C., R. V. Morris, and D. S. McKary (1996), An experimental analog to maturing lunar soil, *Lunar Planet. Sci.*, 27, 13–14.
- Arvidson, R., G. Crozaz, R. J. Droz, C. M. Hohenberg, and C. J. Morgan (1975), Cosmic ray exposure ages of features and events at the Apollo landing sites, *Moon*, 13, 259–267.
- Bell, P. M., H. K. Mao, and R. A. Weeks (1976), Optical spectra and electron paramagnetic resonance of lunar and synthetic glasses: A study of the effects of controlled atmosphere, composition, and temperature, *Proc. Lunar Planet. Sci. Conf.*, 7th, 2543–2559.
- Blewett, D. T., E. I. Coman, B. R. Hawke, J. J. Gillis-Davis, M. E. Purucker, and C. G. Hughes (2011a), Lunar swirls: Examining crustal magnetic anomalies and space weathering trends, *J. Geophys. Res.*, 116, E02002, doi:10.1029/2010JE004656.
- Blewett, D. T., B. W. Denevi, S. J. Lawrence, and E. I. Coman (2011b), Spectra of lunar glass simulants: New and old data for reflectance modeling, *Lunar Planet. Sci. Conf.*, 42, Abstract 1044.
- Boyd, A. K., M. S. Robinson, and H. Sato (2012), Lunar Reconnaissance Orbiter Wide Angle Camera photometry: An empirical solution, *Lunar Planet. Sci. Conf.*, 43, Abs. 2795.
- Bray, V. J., et al. (2010), New insight into lunar impact melt mobility from the LRO camera, *Geophys. Res. Lett.*, 37, L21202, doi:10.1029/2010GL044666.
- Britt, D. T., and C. M. Pieters (1994), Darkening in black and gas-rich ordinary chondrites—The spectral effects of opaque morphology and distribution, *Geochim. et Cosmochim. Acta*, 58(18), 3905–3919.
- Charette, M. P., T. B. McCord, C. M. Pieters, and J. B. Adams (1974), Application of remote spectral reflectance measurements to lunar geology classification and determination of titanium content of lunar soils, *J. Geophys. Res.*, 79(11), 1605–1613, doi:10.1029/JB079i011p01605.
- Cintala, M. J. (1992), Impact-induced thermal effects in the lunar and mercurian regoliths, *J. Geophys. Res.*, 97, 947–973, doi:10.1029/91JE02207.
- Denevi, B. W., et al. (2012), Physical constraints on impact melt properties from Lunar Reconnaissance Orbiter Camera images, *Icarus*, 219(2), 665–675, doi:10.1016/j.icarus.2012.03.020.
- El-Baz, F. (1972), The Alhazen to Abul Wafa swirl belt: An extensive field of light-colored, sinuous markings, *Apollo 16 Prelim. Sci. Rep.*, NASA SP-315, 29–93–29–97.
- Fischer, E. M., and C. M. Pieters (1994), Remote determination of exposure degree and iron concentration of lunar soils using VIS-NIR spectroscopic methods, *Icarus*, 111, 475–488.
- Garrick-Bethell, I., J. W. Head, and C. M. Pieters (2011), Spectral properties, magnetic fields, and dust transport at lunar swirls, *Icarus*, 212(2), 480–492, doi:10.1016/j.icarus.2010.11.036.
- Hapke, B. (1966), Optical properties of the Moon's surface, in *The Nature of the Lunar Surface*, edited by W. Hess, D. Menzel, and J. O'Keefe, pp. 141–154, Johns Hopkins Univ. Press, Baltimore, Md.
- Hapke, B. (1973), Darkening of silicate rocks by solar wind sputtering, *Moon*, 7, 342–355.
- Hapke, B. (2001), Space weathering from Mercury to the asteroid belt, *J. Geophys. Res.*, 106(E5), 10,039–10,073, doi:10.1029/2000JE001338.
- Hapke, B., W. Cassidy, and E. Wells (1975), Effects of vapor-phase deposition processes on the optical, chemical, and magnetic properties of the lunar regolith, *Moon*, 13, 339–353.
- Haskin, L. A., P. A. Helmke, and D. P. Blanchard (1973), Major and trace element abundances in samples from the lunar highlands, *Proc. Lunar Sci. Conf.*, 4th, 1275–1296.
- Hawke, B. R., and J. W. Head (1977), Impact melt on lunar crater rims, in *Impact and Explosion Cratering: Planetary and Terrestrial Implications*, pp. 815–841, Pergamon Press, New York.
- Hawke, B. R., P. G. Lucey, J. F. Bell, and R. Jaumann (1986), Spectral reflectance studies of Tycho crater: Preliminary results, *Proc. Lunar Planet. Sci. Conf.*, 17, 999–1000.
- Hawke, B. R., D. T. Blewett, P. G. Lucey, G. A. Smith, J. F. Bell, B. A. Campbell, and M. S. Robinson (2004), The origin of lunar crater rays, *Icarus*, 170(1), 1–16.
- Hendrix, A. R., and F. Vilas (2006), The effects of space weathering at UV wavelengths: S-class asteroids, *Astron. J.*, 132, 1396–1404.
- Hendrix, A. R., et al. (2012), The lunar far-UV albedo: Indicator of hydration and weathering, *J. Geophys. Res.*, 117, E12001, doi:10.1029/2012JE004252.
- Hood, L. L., and G. Schubert (1980), Lunar magnetic anomalies and surface optical properties, *Science*, 208, 49–51.
- Hood, L. L., and C. R. Williams (1989), The lunar swirls: Distribution and possible origins, *Proc. Lunar Planet. Sci. Conf.*, 19th, 99–113, Houston, Tex.
- Hood, L. L., P. J. Coleman, and D. E. Wilhelms (1979), Lunar nearside magnetic anomalies, *Science*, 204, 53–57.
- Johnson, J. R., and F. Hörz (2003), Visible/near-infrared spectra of experimentally shocked plagioclase feldspars, *J. Geophys. Res.*, 108(E11), 5120, doi:10.1029/2003JE002127.
- Isaacson, P. J., A. B. Sarbadhikari, C. M. Pieters, R. L. Klima, T. Hiroi, Y. Liu, and L. A. Taylor (2011), The lunar rock and mineral characterization consortium: Deconstruction and integrated mineralogical, petrologic, and spectroscopic analyses of mare basalts, *Meteorit. Planet. Sci.*, 46(2), 228–251, doi:10.1111/j.1945-5100.2010.01148.x.
- Keller, L., and D. McKay (1993), Discovery of vapor deposits in the lunar regolith, *Science*, 261, 1305–1307.
- Keller, L., and D. McKay (1997), The nature and origin of rims on lunar soil grains, *Geochim. Cosmochim. Acta*, 61, 2331–2340.
- Keller, L. P., S. J. Wentworth, and D. S. McKary (1998), Space weathering: Reflectance spectroscopy and TEM analysis of individual lunar soil grains, *Lunar Planet. Sci. XXIX*, Abstract #1762.
- Kerridge, J. F. (1994), Production of superparamagnetic Fe⁰ on the lunar surface, *Lunar Planet. Sci.*, XXV, 695–696.
- Kramer, G. Y., et al. (2011), M³ spectral analysis of lunar swirls and the link between optical maturation and surface hydroxyl formation at magnetic anomalies, *J. Geophys. Res.*, 116, E00G18, doi:10.1029/2010JE003729.
- Lawrence, D. J., W. C. Feldman, R. C. Elphic, R. C. Little, T. H. Prettyman, S. Maurice, P. G. Lucey, and A. B. Binder (2002), Iron abundances on the lunar surface as measured by the Lunar Prospector gamma-ray and neutron spectrometers, *J. Geophys. Res.*, 107(E12), 5130, doi:10.1029/2001JE001530.

- Lindstrom, M. M., D. F. Nava, D. J. Lindstrom, S. R. Winzer, R. K. L. Lum, P. J. Schuhmann, S. Schuhmann, and J. A. Philpotts (1977), Geochemical studies of the white breccia boulders at North Ray Crater, Descartes region of the lunar highlands, *Proc. Lunar Planet. Sci. Conf.*, 8th, 2137–2151.
- Lucey, P. G., and M. A. Riner (2011), The optical effects of small iron particles that darken but do not redden: Evidence of intense space weathering on Mercury, *Icarus*, 212(2), 451–462, doi:10.1016/j.icarus.2011.01.022.
- Lucey, P. G., G. J. Taylor, and E. Malaret (1995), Abundance and distribution of iron on the Moon, *Science*, 268, 1150–1153.
- Lucey, P. G., D. T. Blewett, G. J. Taylor, and B. R. Hawke (2000a), Imaging of lunar surface maturity, *J. Geophys. Res.*, 105(E8), 20,377–20,386, doi:10.1029/1999JE001110.
- Lucey, P. G., D. T. Blewett, and B. L. Jolliff (2000b), Lunar iron and titanium abundance algorithms based on final processing Clementine UVVIS images, *J. Geophys. Res.*, 105(E8), 20,297–20,305, doi:10.1029/1999JE001117.
- Lue, C., Y. Futaana, S. Barabash, M. Wieser, M. Holmström, A. Bhardwaj, M. B. Dhanya, and P. Wurz (2011), Strong influence of lunar crustal fields on the solar wind flow, *Geophys. Res. Lett.*, 38, L03202, doi:10.1029/2010GL046215.
- Milton, D. J., and P. S. de Carli (1963), Maskelynite: Formation by explosive shock, *Science*, 140(3567), 670–671.
- Morota, T., et al. (2009), Formation age of the lunar crater Giordano Bruno, *Meteorit. Planet. Sci.*, 44(8), 1115–1120, doi:10.1111/j.1945-5100.2009.tb01211.x.
- Morris, R. V. (1976), Surface exposure indices of lunar soils—A comparative FMR study, *Proc. Lunar Planet. Sci. Conf.*, 7th, 315–335.
- Morris, R. V. (1978), The surface exposure (maturity) of lunar soils: some concepts and I_0/FeO compilation, *Proc. Lunar Planet. Sci. Conf.*, 9th, 2287–2297.
- Noble, S. K., C. M. Pieters, and L. P. Keller (2007), An experimental approach to understanding the optical effects of space weathering, *Icarus*, 192, 629–642.
- Oberbeck, V. R. (1975), The role of ballistic erosion and sedimentation in lunar stratigraphy, *Rev. Geophys. Space Phys.*, 13, 337–362.
- Oberbeck, V. R., F. Hörz, R. H. Morrison, W. L. Quaide, and D. E. Gault (1975), On the origin of the lunar smooth plains, *Moon*, 12(1), 19–54.
- Pieters, C. M. (1977), Characterization of lunar mare basalt types. II: Spectral classification of fresh mare craters, *Proc. Lunar Sci. Conf.*, 8th, 1037–1048.
- Pieters, C. M. (1996), Plagioclase and maskelynite diagnostic features, *Lunar Planet. Sci.*, 27, 1031–1032.
- Pieters, C. M., and T. Hiroi (2004), RELAB (Reflectance Experiment Laboratory): A NASA multiuser spectroscopy facility, *Lunar Planet. Sci.*, 35, Abs. 1720.
- Pieters, C. M., J. B. Adams, P. J. Mouginiis-Mark, S. H. Zisk, M. O. Smith, J. W. Head, and T. B. McCord (1985), The nature of crater rays: The Copernicus example, *J. Geophys. Res.*, 90(B14), 12,393–12,413, doi:10.1029/JB090iB14p12393.
- Pieters, C. M., E. M. Fischer, O. Rode, and A. Basu (1993), Optical effects of space weathering: The role of the finest fraction, *J. Geophys. Res.*, 98(E11), 20,817–20,824, doi:10.1029/93JE02467.
- Pieters, C. M., L. Taylor, S. Noble, L. Keller, B. Hapke, R. Morris, C. Allen, D. McKay, and S. Wentworth (2000a), Space weathering on airless bodies: Resolving a mystery with lunar samples, *Meteorol. Planet. Sci.*, 35, 1101–1107.
- Pieters, C. M., L. A. Taylor, D. McKay, S. Wentworth, R. Morris, and L. Keller (2000b), Spectral characterization of lunar mare soils, *Lunar Planet. Sci. Conf.*, 31, Abs. 1865.
- Robinson, M. S., et al. (2010), Lunar Reconnaissance Orbiter Camera (LROC) overview, *Space Sci. Rev.*, 150, 81–124, doi:10.1007/s11214-010-9634-2.
- Roddy, D. J., R. O. Pepin, and R. B. Merrill (1977), Impact and explosion cratering: Planetary and terrestrial implications, in *Proceedings of the Symposium on Planetary Cratering Mechanics, Flagstaff, Ariz.*, pp. 1315, Pergamon Press, New York, 13–17 Sept.
- Sasaki, S., K. Nakamura, Y. Hamabe, E. Kurahashi, and T. Hiroi (2001), Production of iron nanoparticles by laser irradiation in a simulation of lunar-like space weathering, *Nature*, 410(6828), 555–557.
- Schaber, G. G., D. R. Scott, and J. B. Irwin (1972), Glass in the bottom of small lunar craters: An observation from Apollo 15, *Geol. Soc. Am. Bull.*, 83, 1573–1578.
- Scholten, F., J. Oberst, K.-D. Matz, T. Roatsch, M. Wählisch, E. J. Speyerer, and M. S. Robinson (2012), GLD100: The near-global lunar 100 m raster DTM from LROC WAC stereo image data, *J. Geophys. Res.*, 117, E00H17, doi:10.1029/2011JE003926.
- Schultz, P. H., and L. J. Srnka (1980), Cometary collisions on the Moon and Mercury, *Nature*, 284, 22–26.
- Smrekar, S., and C. M. Pieters (1985), Near-infrared spectroscopy of probable impact melt from three large lunar highland craters, *Icarus*, 63(3), 442–452.
- Starukhina, L. V., and Y. G. Shkuratov (2004), Swirls on the Moon and Mercury: Meteoroid swarm encounters as a formation mechanism, *Icarus*, 167(1), 136–147.
- Taylor, L. A., C. M. Pieters, L. P. Keller, R. V. Morris, and D. S. McKay (2001), Lunar mare soils: Space weathering and the major effects of surface-correlated nanophase Fe, *J. Geophys. Res.*, 106(E11), 27,985–27,999, doi:10.1029/2000JE001402.
- Taylor, L. A., C. Pieters, A. Patchen, D.-H. S. Taylor, R. V. Morris, L. P. Keller, and D. S. McKay (2010), Mineralogical and chemical characterization of lunar highland soils: Insights into the space weathering of soils on airless bodies, *J. Geophys. Res.*, 115, E02002, doi:10.1029/2009JE003427.
- Trask, N. J. (1971), Geologic comparisons of mare materials in the lunar equatorial belt, including Apollo 11 and Apollo 12 landing sites, in *Geological Survey Research, U.S. Geol. Surv. Prof. Paper 750-D*, pp. D138–D144.
- Vernazza, P., R. P. Binzel, A. Rossi, M. Fulchignoni, and M. Birlan (2009), Solar wind as the origin of rapid reddening of asteroid surfaces, *Nature*, 458, 993–995.
- Wagner, J. K., B. W. Hapke, and E. N. Wells (1987), Atlas of reflectance spectra of terrestrial, lunar, and meteoritic powders and frosts from 92 to 1800 nm, *Icarus*, 69, 14–28.
- Wells, E., and B. Hapke (1977), Lunar soil: Iron and titanium bands in the glass fraction, *Science*, 195, 977–979.
- Wells, E. N. (1977), Optical absorption bands in glasses of lunar composition, PhD dissertation, University of Pittsburgh, Pittsburgh, Pa.
- Wieser, M., S. Barabash, Y. Futaana, M. Holmström, A. Bhardwaj, R. Sridharan, M. B. Dhanya, A. Schaufelberger, P. Wurz, and K. Asamura (2010), First observation of a mini-magnetosphere above a lunar magnetic anomaly using energetic neutral atoms, *Geophys. Res. Lett.*, 37, L05103, doi:10.1029/2009GL041721.
- Wilshire, H. G., and H. J. Moore (1974), Glass-coated lunar rock fragments, *J. Geol.*, 82, 403–417.
- Yamada, M., S. Sasaki, A. Fujiwara, T. Hiroi, S. Hasegawa, H. Nagahara, H. Ohashi, H. Ohtake, and H. Yano (1999), Simulation of space weathering by nanosecond pulse laser heating and proton implantation: Difference of olivine and pyroxene samples, *Lunar Planet. Sci.*, 30, Abs. 1566.
- Yin, L., and T. Tsang (1976), On the ion bombardment reduction mechanism, *Geochem. Cosmochim. Acta*, 7, 891–900.
- Yin, L., S. Ghose, and I. Adler (1972), Investigation of a possible solar wind darkening of the lunar surface by photoelectron spectroscopy, *J. Geophys. Res.*, 77, 1360–1367, doi:10.1029/JB077i008p01360.
- Yin, L., T. Tsang, and I. Adler (1975), ESCA studies on solar wind reduction mechanisms, *Geochem. Cosmochim. Acta*, 6, 3277–3284.